Observed and Modelled Mixed-Layer Properties on the Continental Shelf of Sardinia (Mediterranean Sea)

Reiner Onken[1]

[1]Helmholtz-Zentrum Geesthacht Centre for Materials und Coastal Research (HZG), Max-Planck-Straße 1, 21502 Geesthacht, Germany

Correspondence to: Reiner.Onken@hzg.de

Abstract. The *Regional Ocean Modeling System* (ROMS) has been employed to explore the sensitivity of the forecast skill of mixed-layer properties to the initial conditions, boundary conditions, and vertical mixing parameterisations. The initial and lateral boundary conditions were provided by the *Mediterranean Forecasting System* (MFS) or by the MERCATOR global ocean circulation model via one-way nesting; the initial conditions were additionally updated by the assimilation of observations. Nowcasts and forecasts from the weather forecast models COSMO-ME and COSMO-IT, partly melded with observations, served as surface boundary conditions. The vertical mixing was parameterised by the GLS (*Generic Length Scale*) scheme (Umlauf and Burchard, 2003) in four different setups. All ROMS forecasts were validated against observations which were taken during the REP14-MED oceanographic survey to the west of Sardinia. Nesting ROMS in MERCATOR and updating the initial conditions by data assimilation provided the best agreement of the predicted mixed-layer temperature and the mixed-layer depth with time series from a moored thermistor chain. Further improvement was obtained by the usage of COSMO-ME atmospheric forcing which was melded with real observations, and by the application of the $k - \epsilon$ vertical mixing scheme with increased vertical eddy diffusivity. The predicted temporal variability of the mixed-layer temperature was reasonably well correlated with the observed variability in the frequency range above one cycle per day, while the modelled variability of the mixed-layer depth exhibited only agreement with the observations near the diurnal frequency peak. For the forecasted horizontal variability, reasonable agreement was found with observations from a ScanFish section, but only for the mesoscale wavenumber band; the observed sub-mesoscale variability was not reproduced by ROMS.

1 Introduction

In ocean acoustics research, the diagnostics and prediction of selected mixed-layer properties – such as the mixed-layer depth and the mixed-layer temperature – is of primary interest because they have a profound impact on the propagation of sound in the ocean. In this article, a high-resolution ocean circulation numerical model is presented which provides nowcasts and forecasts of these properties. The objectives are (i) to evaluate the sensitivity of the properties to different setups of initial conditions, lateral boundary conditions, atmospheric forcing patterns, and vertical mixing parameterisations, and (ii) to find a setup which reproduces and predicts best the depth and the temperature of the mixed-layer and their associated spatio-temporal variabilities obtained from observations.

By definition, temperature and salinity are constant in the mixed-layer and the sound speed increases slightly with depth due to the pressure effect (Dietrich et al., 1975). Therefore, sound rays in the mixed-layer are refracted upwards and reflected at the sea surface. Hence, the mixed-layer acts as a *surface duct* (Katsnelson et al., 2012). On the other hand, at depth greater than the mixed-layer depth and because of the decreasing temperature, the rays are refracted in the other direction, i.e. towards

5   greater depths. Consequently in terms of passive acoustic monitoring, if a sound source is within the mixed-layer, the sound cannot be "heard" at depths greater than the mixed-layer depth, and if the sound source is located below the mixed-layer, it cannot be heard in the mixed-layer. The equivalent is true for the location of objects by active sonar – if the sonar is within the mixed-layer, the acoustic signal can hardly reach an object at greater depth, and vice versa. This is, of course, an idealised model based on ray theory which does not take account of non-linear and frequency dependent effects, but it clearly emphasises

10   that knowledge about the depth of the mixed-layer is mandatory for the planning and conduction of acoustic experiments.

The sound speed c in seawater is a function of temperature T, salinity S, and the pressure p. Hence, small changes dc of the sound speed can be described by the total differential

$$dc = \left.\frac{\partial c}{\partial T}\right|_{S_0,p_0} dT + \left.\frac{\partial c}{\partial S}\right|_{T_0,p_0} dS + \left.\frac{\partial c}{\partial p}\right|_{T_0,S_0} dp \tag{1}$$

where the subscripts T_0, S_0, p_0 indicate that T, S, and p, respectively, are held constant during the execution of the partial

15   differential. For mid-latitudes and close to the sea surface ($T_0 = 15°\,\mathrm{C}$, $S_0 = 35$, $p_0 = 0$ dbar), the partial differentials in Eq. (1) yield $\partial c/\partial T \approx 3.2\ \mathrm{m\,s^{-1}K^{-1}}$, $\partial c/\partial S \approx 1.2\ \mathrm{m\,s^{-1}}$ which means that the fractional change of the sound speed with temperature is about three times larger than the change with salinity (Chen and Millero, 1977). Moreover, as typical spatio-temporal variations of temperature are $\mathcal{O}(10\ \mathrm{K})$ but those of salinity only $\mathcal{O}(1)$ at best, the first two terms in Eq. (1) yield as $31.2\ \mathrm{m\,s^{-1}}$ and $1.2\ \mathrm{m\,s^{-1}}$. Hence, changes of the sound speed are largely controlled by changes of the temperature, and the

20   impact of salinity variations in the mixed-layer can confidently be ignored for the calculation of the sound speed. However, one may note that this is only true for the open ocean. In coastal areas, estuaries, and in polar regions, the salinity variations are frequently larger and the concurrent variations of temperature smaller.

Besides the temperature and the depth of the mixed-layer, the temporal and horizontal variability of these two quantities require special attention (Pace and Jensen, 2002). The temporal variability at a fixed location is affected by temporal changes

25   of

- Air-sea fluxes of momentum, heat, and fresh water,
- Activities of surface waves and internal waves,
- Horizontal advection,
- Vertical motion, and

30   - Optical properties of the seawater.

The horizontal variability is due to spatial differences of the same quantities and in addition by the presence of mesoscale and sub-mesoscale features like fronts, meanders, eddies, and filaments (e.g. Medwin and Clay (1998)). Both the temporal and the horizontal variability are impacting the sound speed and the underwater sound propagation.

The experimental area addressed in this study is situated in the Mediterranean Sea to the west of Sardinia. Here, an oceanographic survey took place in June 2014 (Onken et al. (2014), Onken et al. (2016)) the observational data of which will be used to drive the aforementioned ocean circulation model and to validate the model results.

The reader may note that within this article all dates refer to the year 2014 and all times are in UTC (*Universal Time Coordinated*) except where otherwise stated.

2   Observational data

The observational data originate from the REP14-MED experiment which took place in the eastern Sardo-Balearic Sea in the period of time 6–25 June 2014. The collection of in situ data was accomplished by the NATO Research Vessel *Alliance*, the Research Vessel *Planet* of the German Ministry of Defence, a fleet of underwater gliders, surface drifters, one sub-surface float, and six oceanographic moorings. Throughout this article however, the author will refer only to the data of one mooring denoted as *M1*, and to the CTD (*Conductivity-Temperature-Depth*) data collected by the survey vessels and the gliders. For more details of the observations, see Onken et al. (2016).

2.1   Mooring M1

M1 (Fig. 1) was launched on 8 June at 7:14 at 8°12.98' E, 39°30.80' N (Fig. 2) and recovered on 20 June at 13:55. The water depth at the launch position was ≈150 m. M1 consisted of the central mooring $M1_{CTR}$ and a sideways extending appendix $M1_{APP}$ floating at the sea surface. $M1_{CTR}$ was equipped with an upward-looking ADCP (*Acoustic Doppler Current Profiler*) mounted at a nominal depth of 100 m below the sea surface, a CTD probe at 1 m depth, and with a meteorological buoy at the surface. The appendix was connected by a 50 m long rope to $M1_{CTR}$ and extended to about 40 m in the vertical direction. 40 Starmon temperature recorders were densely spaced along the vertical cable in order to record the temperature with high vertical resolution. In addition, four RBR data loggers were mounted on the cable for determination of the actual depth of the Starmons. Their nominal and actual vertical positions and the recorded parameters are summarised in Table 1.

The Starmons recorded time t and temperature T, and the RBRs in addition pressure p, both in intervals of about 10 s. The depth z was calculated internally by the RBR software. As the Starmons did not have a pressure gauge, their actual vertical position was evaluated thereafter from the depth records of the RBRs because the positions of the Starmons relative to the RBRs was known. This was accomplished in the following way:

- The RBR depth records were clipped on 8 June 07:18 and 20 June 13:30, and then sub-sampled in 5-minutes intervals.
- At each instant, a second order polynomial fit was applied to the actual depth versus the nominal depth.
- The Starmon records at 3.0 m and 7.0 m depth were rejected because the recorders failed (cf. sensor positions 7 and 15 in Table 1).
- The actual depths of the Starmon recorders were calculated with a polynomial using the previously calculated coefficients.

This procedure was advisable in order to correct for potential depth changes of the Starmons due to the actions of waves, internal waves, horizontal advection, and vertical shear. However, it turn out that these corrections were rather small: right at the sea surface at sensor position 1, the actual depth of the Starmon (cf. Table 1) varied between 0 and 1.85 m, and the depth of the sensors at position 41 varied between 39.89 and 41.81 m. Hence, the applied corrections were around ± 1 m.

5   In Fig. 10, several properties of the near-surface layers (at this instant the expression *mixed-layer* is avoided because sometimes there is no mixed-layer) are illustrated, the behaviour of which may be difficult to be reproduced by the circulation model:

  – The near-surface temperature (Fig. 10a) varied between about 22°C and more than 24°C. At the begin of the recording period, it was around 23°C, then it rose slowly and reached the maximum value on 12 and 14 June, and afterwards it
10   decreased. The minimum around 22°C was reached on 17 June, and during the final three days, the temperature rose again by about 1°K.

  – The mixed-layer depth may be defined by means of that depth where the vertical temperature gradient is maximal (Fig. 10d). Between about 15 and 20 June, there is clear evidence for such a signal – the mixed-layer depth varied between about 4 m on 15 June and about 13 m on 18 and 19 June. However, between 8 and 14 June, the signal is rather indistinct:
15   the night-time mixed-layer depth ranged from about 2 m on 9 June to about 6 m on 10 June, but during daylight hours the maximum gradient was sometimes found right at the surface; thus a mixed-layer in the "classical" sense did not exist.

  – There are clear signals of the temporal variability, both for temperature and the depth of the mixed-layer. The variability occurred on all scales between about two weeks and the Nyquist period of 10 minutes (twice the sampling interval; see above).

20 **2.2   Data collected by lowered CTD, gliders and towed measuring systems**

On both survey vessels, casts with lowered CTD probes were conducted during the entire survey, but here only those casts are referred to which were taken 7–11 June. These casts belonged to the initialisation survey, the purpose of which was to provide realistic temperature and salinity data for the initialisation of numerical models. In total, 108 casts were taken on a regular horizontal grid with a mesh size of ≈10 km (Fig. 2), resolving the internal Rossby radius of deformation. Eleven gliders were
25 deployed on 8 and 9 June, respectively, at the positions marked "L" in Fig. 3, and afterwards directed to their nominal zonal tracks. The scheduled tracks were arranged parallel to the CTD sections (Fig. 2) but offset by 5 km in the meridional direction. For the validation of model forecasts, *Alliance* conducted a survey 21–24 June with a ScanFish. The tracks are shown in Fig. 4.

3 The circulation model

3.1 ROMS

The employed numerical ocean circulation model is ROMS, the *Regional Ocean Modeling System*. ROMS is a hydrostatic, free-surface, primitive equations ocean model, the algorithms of which are described in detail in Shchepetkin and McWilliams
(2003) and Shchepetkin and McWilliams (2005). In the vertical, the primitive equations are discretised over variable topography using stretched terrain-following coordinates, so-called *s-coordinates* (Song and Haidvogel, 1994). In this article, spherical coordinates on a staggered Arakawa C-grid are applied in the horizontal, and the horizontal mixing of momentum and tracers is along isopycnic surfaces. The vertical mixing is parameterised by means of the GLS *Generic Length Scale* scheme developed by Umlauf and Burchard (2003). The air-sea interaction boundary layer in ROMS is based on the bulk parameterisation of
Fairall et al. (1996).

3.2 The model domain, discretisation

The model domain is situated to the west of Sardinia (Fig. 5). The west and east boundaries are at 6°30.5' E and 8°35.5' E, while in the south and north the domain is limited by the 38°36.4' N and 40°59.6' N latitude circles, respectively. In east-west direction, the domain is separated in 120 grid cells, and in south-north direction in 178 cells, which yields an average grid
spacing of $\Delta x \approx \Delta y \approx 1500\,\mathrm{m}$ in the zonal and meridional direction, respectively. A comparison with Fig. 2 reveals that the domain boundaries are kept away from the observations by about 30 arc minutes; this was intended in order to mitigate a deterioration of the model solution at the observational sites due to false advection from the open boundaries.

Bathymetry data from the *General Bathymetric Chart of the Oceans* (GEBCO) with a spatial resolution of one arc minute were provided by the *British Oceanographic Data Centre* (BODC), and coastline data were obtained from NOAA (*National
Oceanic and Atmospheric Administration*). In order to avoid crowding of the s-coordinates in shallow water regions, the bathymetry was clipped at 20 m which is the minimum allowed water depth, and for the smoothing of the bathymetry, a second-order Shapiro filter was applied.

In the vertical direction, the model domain was separated in 70 s-layers, the position of which is controlled by three parameters $(\theta_s, \theta_b, h_c)$ and two functions, V_{tr}, V_{str}. Here, V_{tr} is the *transformation equation*, V_{str} the *vertical stretching function*, θ_s
and θ_b are the *surface and bottom control parameters*, and h_c is the *critical depth* controlling the stretching (for more details, see `https://www.myroms.org/wiki/`). For all ROMS runs shown below, the functions and parameters were selected as $V_{tr} = 2, V_{str} = 1, \theta_s = 3, \theta_b = 0.4$, while h_c was kept variable.

3.3 Initialisation

ROMS was initialised from nowcasts of the coarser *Mediterranean Forecasting System* (MFS, Dobrowsky et al. (2009), Tonani et al.
(2014) or the MERCATOR global ocean circulation model (Drévillon et al., 2008) via downscaling. In either case, the downscaling from the *parent* to the *child* was accomplished first by linear horizontal interpolation of the prognostic fields on the

ROMS grid. As the maximum horizontal resolution of MFS is close to 7 km (1/16°) and that of MERCATOR is 9.25 km (1/12°), the scale factors were around 4.7 and 6.2, respectively. Thereafter, all fields were interpolated vertically from the horizontal depth levels to the s-coordinates. A special issue was the alignment of the land masks of the parent and the child: if any wet grid cell of the child was covered by a dry grid cell of the parent, a smooth transition of all variables was created by taking the

5 average of the surrounding parent cells. However, as this may lead to a violation of continuity by non-zero horizontal velocities normal to the land mask, all horizontal velocities next to the ROMS land mask were set to zero.

3.4 Lateral boundary conditions and nesting

The ROMS code includes various methods for the treatment of open boundaries. After extensive sensitivity studies, it was found that the following algorithms served best for the posed problem: for the sea surface elevation, the *Chapman condition*

10 was selected (Chapman, 1985), and for all other quantities (i.e. barotropic and baroclinic momentum, turbulent kinetic energy, temperature, and salinity), the *mixed radiation-nudging conditions* after Marchesiello et al. (2001) were applied.

The lateral time-dependent boundary conditions were provided by the parent by means of one-way nesting. However, the information from the parent was not instantaneously superimposed to the ROMS solution but an additional nudging was applied to all prognostic variables (except for the sea surface elevation) which allowed these fields to adjust slowly to the parent values

15 at the boundaries within an e-folding time scale of two days. In addition, a factor 5 was used for the nudging time scales which causes a stronger nudging on the inflow.

3.5 Surface boundary conditions

At the sea surface, boundary conditions for the air-sea exchange of fresh water, momentum, and heat were evaluated from the outputs of two numerical weather prediction models and from the measurements of the meteorological buoy on top of M1 (see

20 Fig. 1) by means of the wind field at 10 m (2 m for M1) height, air temperature and relative humidity at 2 m, air pressure at sea level, cloudiness (not available from M1), short wave radiation, and precipitation. The output of the weather prediction models was made available by the Italian Weather Service CNMCA (*Centro Nazionale di Meteorologia e Climatologia Aeronautica*) in two different setups, COSMO-ME and COSMO-IT. COSMO-ME covers the entire Mediterranean Sea with a horizontal resolution of 7 km and provided 72-hr forecasts, while COSMO-IT encompasses Italy and the adjacent waters at the very high

25 resolution of 2.2 km but the forecast range was only 24 hr. The temporal resolution of both models was 1 hr. The time series of all available variables from COSMO-ME, COSMO-IT, and the meteorological buoy are shown in Fig. 6 for the period of time 7–25 June at the M1 position.

3.6 Data assimilation

In most of the model runs presented below, temperature and salinity data from shipborne CTD probes and gliders were as-

30 similated. Namely, ROMS includes a module which enables data assimilation by the *4D-Var* method. However, as 4D-Var is based on variational methods it is very expensive in terms of computer resources. Therefore, *Objective Analysis* (OA, see

Bretherton et al. (1976), Carter and Robinson (1987)) was the selected method for data assimilation. During the integration of ROMS, the engine conducting the data assimilation was invoked every day at midnight, and it was controlled by six parameters:

- W: the width of the time window which determines what data are assimilated. In all ROMS runs below, $W = 48$ hr. Hence, all temperature and salinity data of the previous and the following 24 hr were selected for assimilation.

- C: the isotropic correlation length scale. $C = 15$ km was used throughout which is approximately the internal Rossby radius of the Western Mediterranean in summer (Grilli and Pinardi, 1998).

- δT_{obs}, δS_{obs}: the *observational errors* of temperature and salinity, respectively. $\delta T_{obs} = 0.5$ K and $\delta S_{obs} = 0.16$ were used throughout. These values were obtained from the variance of all CTD casts in the upper thermocline.

- δT_{clim}, δS_{clim}: the *climatology errors*; $\delta T_{clim} = 5 \times \delta T_{obs} = 2.5$ K and $\delta S_{clim} = 5 \times \delta S_{obs} = 0.8$ were applied.

10 ## 3.7 Integration and output

All ROMS runs presented below were initialised on 1 June 00:00 and integrated forward for 24 days until 25 June 00:00. To satisfy the horizontal and the vertical CFL criterion, a baroclinic time step $\Delta t = 108$ s (800 steps per day) was chosen, and the number of barotropic time steps between each baroclinic time step was 40. Harmonic mixing along isopycnals with an eddy diffusivity coefficient of $10\,\mathrm{m^2\,s^{-1}}$ was used for the horizontal diffusion of the tracers T and S, and a horizontal viscosity

15 coefficient of $50\,\mathrm{m^2\,s^{-1}}$ was selected for the diffusion of momentum. Further on, a quadratic law using a coefficient of 0.003 was applied for the bottom friction, and the pressure gradient term was computed using the standard density Jacobian algorithm of Shchepetkin and Williams (2001, unpublished; see

`http://www.atmos.ucla.edu/~alex/ROMS/pgf1A.ps`).

The three-dimensional volume of all prognostic fields was written to an output file at 6-hr intervals. For comparison of the

20 ROMS results with the observed records at mooring M1, time series of vertical temperature profiles right at the position of M1 where written to an extra file at the full temporal resolution.

4 Sensitivity of near-surface temperature and mixed-layer depth

In this section are investigated the impacts of

- initialising ROMS from different data sets,

- the setup of the vertical grid

- different atmospheric forcing patterns,

- different vertical mixing schemes

- the background eddy diffusivity

on the near-surface temperature and the depth of the mixed-layer. This was achieved by five series of ROMS runs named A–E.

30 The task of each series was to assess the sensitivity of the ROMS forecast skill to variations of the mechanisms mentioned in

the bullets above. For each run, the ability of ROMS to predict the temperature was assessed by means of the root-mean-square (*rms*) difference

$$\Delta T = \left[\frac{1}{N} \sum_1^N (T_{ROMS} - T_{obs})^2 \right]^{\frac{1}{2}} \tag{2}$$

between the observed temperature T_{obs} and the predicted temperature T_{ROMS} at the N actual depths of the observations. ΔT was evaluated for the period of time 12 June 00:00–20 June 13:55 where observations were available in 5-minute intervals (cf. Section 2.1). This interval was selected because it enabled the comparison of all runs with those which were forced by data assimilation until 12 June 00:00. In order to synchronise the modelled and the observed temperature, T_{ROMS} was linearly interpolated in space and time on the observations. The equivalent method was also applied to the mixed-layer depth, D, which due to the lack of salinity observations was defined as that depth where the temperature was for the first time by 1 K colder than the temperature at the surface, hence

$$\Delta D = \left[\frac{1}{N} \sum_1^N (D_{ROMS} - D_{obs})^2 \right]^{\frac{1}{2}} \tag{3}$$

is the *rms* difference of the mixed-layer depth.

4.1 Series A: initialising ROMS from different data sets

In this series, $h_c = 200\,\mathrm{m}$ was selected for the critical depth. In the first run, referred to as A1, ROMS was initialised from MFS while in A2, the initial conditions were provided by MERCATOR. A3 was initialised from MERCATOR as well but in addition, temperature and salinity data from CTD casts and 10 gliders were assimilated which were taken 7–12 June 00:00 (cf. Section 2.2 and Figs. 2, 3, 7). The surface boundary conditions of all runs in the A-series were provided by COSMO-ME.

In Fig. 8a are shown time series of the near surface temperatures in runs A1–A3, in comparison with the corresponding observations of the uppermost Starmon sensor in M1 at the same depth level. In A1 and A2, the predicted temperatures agree reasonably well with the observations of 8–10 June and after 15 June, but in the period between, the temperature exceeds the observation by several degrees. Fig. 6 shows that during this period the predicted and observed wind speeds were close to $0\,\mathrm{m\,s^{-1}}$ and the short-wave radiation flux reached maximum values of more than $800\,\mathrm{W\,m^{-2}}$. Hence, as these quantities are the major drivers of the mixed-layer temperature, it has to be concluded that the parameterisation of the vertical mixing in ROMS is not adequate for such calm situations. By contrast, as soon as the wind became stronger after 14 June, the maximum difference between the predicted and measured temperature is less than 1 K. In A3, there is also a good agreement between the modelled and the observed temperature before 11 June and after 15 June. However, as can be seen from the sudden drop of the modelled temperature at midnight of 11 June, the data assimilation led to an underestimate of the surface temperature. The reasons for this are twofold: first, some of the assimilated profiles started at 2 m or even 3 m depth because the measurements close to the surface were not reliable. In such cases, the uppermost measurements were extended to the surface and led to an underestimate of the near-surface temperature, which sometimes was significant because of the extremely shallow or even non-existent mixed-layer. And second, the OA "advected" properties from neighbouring casts which were not representative

for the M1 position. On 13 June, the modelled temperature exceeds again the observations by more than 2 K. In order to have an objective measure for the forecasted temperature, ΔT was evaluated for all runs. While $\Delta T \geq 1\,\mathrm{K}$ in A1 and A2, it drops to 0.79 K in A3.

The temporal evolution of the mixed-layer depth is displayed in Fig. 8b. As revealed by the decreasing *rms* differences ΔD between the modelled and observed mixed-layer depths, the forecast skill increases from A1 to A2 and from A2 to A3. Noteworthy is the close agreement between the observed and modelled mixed-layer depth in A3 before 12 June which was forced by the assimilation. Remarkable is again the mismatch between the model and the observations 12–15 June which is another indication for an inadequate parameterisation of the mixed-layer dynamics.

The vertical distribution of the *rms* temperature differences ΔT of all runs of the A-series is shown in Fig. 9. It is demonstrated that at all depth levels except for a narrow range at about 2 m depth, ΔT is lower in A2 compared to A1. The assimilation in A3 led to a further drastic decrease below about 5 m depth and right at the surface. In summary, nesting ROMS in MERCATOR and assimilating CTD profiles provided the best forecasts for the temperature and the depth of the mixed-layer, and the thermocline temperature below about 5 m depth. Therefore, all runs in the B-series will be based on A3.

The temporal evolution of the modelled temperature in A3 at the position of mooring M1 is shown in Fig. 10b. In comparison with Fig. 10a, the modelled temperature close to the sea surface is too high on 13 and 14 June, while at depths greater than about 3 m–10 m, T_{A3} appears too low. This is confirmed by Fig. 10c which exhibits the temperature difference $T_{A3} - T_{M1}$: in approximately the upper 2 m depth range, T_{A3} partly exceeds T_{M1} by about 2 K during these days, and just below, T_{A3} is up to 4 K lower than the observed temperature. This aberrant cold layer can be identified during the whole model run. Apparently, the modelled mixed-layer depth is shallower than the observed one. This is illustrated by the vertical temperature gradient in Fig. 10e. Namely, a comparison with Fig. 10d reveals that the general descending trend of the maximum gradient is similar, but the depth of the modelled maximum is always less than the observed one. Moreover, the observed variability is significantly higher than the modelled one. While for the entire period, there is clear evidence for a strong diurnal variability in the observations (e.g. the deep mixed-layer in the early morning and the shallow mixed-layer in the afternoon), the modelled variability is much less pronounced. Another feature worth mentioning is that the upper thermocline is too warm during the assimilation phase. It has been verified that this was caused by the assimilation of glider data because this feature is not present in a run where only casts from lowered CTD were assimilated (not shown). As can be seen from Figs. 2 and 7, two CTD casts were taken exactly at the M1 position while several glider casts are in close range. Thus, the modelled temperature at M1 was mainly determined by the glider measurements, above all, because the large amount of nearby glider profiles reduced the statistical weight of the CTD casts.

4.2 Series B: sensitivity to the setup of the vertical grid

If the transformation equation and the vertical stretching function are held constant, the layer thicknesses of the ROMS vertical grid is controlled by the surface and bottom control parameters, θ_s and θ_B and the critical depth, h_c. For mixed-layer modelling in shelf areas, it would be desirable to have high vertical resolution close to the surface which can be achieved by either increasing θ_s or decreasing h_c. However, as increasing θ_s would make the vertical transformation more non-linear, it was

decided to keep $\theta_s = 3$ constant and vary only h_c. In this series, the sensitivity of the ROMS results to five different settings of the critical depth is investigated, using $h_c \in \{20, 100, 200, 500, 1000\}$ m. For each of these choices, the impact on the layer thicknesses at the position of mooring M1 is illustrated in Fig. 11. The minimum layer thickness of about 0.8 m right at the sea surface is achieved by $h_c = 20$ m in Run B1, while the thickness of that layer gradually increases in B2–B5. In the latter

5 ($h_c = 1000$ m), the thickness is close to 2 m. B3 being identical to A3 is the control run.

For all runs of this series, the temporal evolution of the mixed-layer properties is displayed in Fig. 12. Although still too high around 14 June, the near-surface temperatures in B1, B2, B3 are most resembling the observations which is also expressed by corresponding low values for ΔT. For the mixed-layer depth, the minimum ΔD values of 2.62 m and 2.66 m were obtained from B3 and B2. Hence, 100 m or 200 m appear to be the right choices for the critical depth parameter h_c, but also in these

10 runs, the modelled mixed-layer depth is by far too shallow 12–15 June and partly during the time thereafter. By contrast in the thermocline, B3–B5 perform slightly better than B1, B2 (Fig. 13); the reason for this behaviour is unknown. Nevertheless, as it is the objective of this study to find a model setup which predicts best the mixed-layer properties, B2 ($h_c = 200$ m) will serve as control run in Series C below.

4.3 Series C: sensitivity to atmospheric forcing

15 Series C consists of three model runs, C1, C2, and C3. C1 is identical to B2; in C2, the surface boundary conditions were provided by COSMO-IT instead of COSMO-ME. And in C3, the atmospheric forcing was defined by means of the observations of the meteorological buoy on top of mooring M1. Here, the observations were spread uniformly across the entire model domain whenever available. If no observations were available, i.e. before 8 June and after 20 June, the atmospheric fields of COSMO-ME were used. As observations of cloudiness were not available from M1, the corresponding fields from COSMO-ME were

20 used throughout.

According to Fig. 14a, the predicted near-surface temperature from C2 resembles closely that of C1, except for 14–16 June where the temperatures in C2 are about 1 K higher. Apparently, this was driven by different wind forecasts of the weather prediction models (cf. Fig. 6). Before 14 June, the wind forecasts of both models were almost identical, but for the following two days during a period of stronger winds, the forecasts differ significantly from each other. Overall, the near-surface temperature

25 does not appear to be very sensitive to the choice of the weather forecast models. This is also expressed by ΔT which attains similar value of 0.70 K in both cases. The signature of the temperature changes considerably when ROMS was driven by the weather observed at M1: this is already evident 8–10 June where the modelled temperature in C3 is different from C1 and C2, respectively. And after 13 June, it it is mostly higher than both the observations and the predictions of C1 and C2, which correspondingly leads to a higher ΔT of 0.78 K. With respect to the modelled mixed-layer depth (Fig. 14b) and based on the

30 ΔD criterion, C1 is superior to C2 and C3, but the large discrepancies 12–15 June between predictions and observation are still present in all three runs. This corroborates the above hypothesis that the mismatch is not caused by the atmospheric forcing because the most appropriate forcing was applied in C3.

A surprising result was obtained from the vertical structure of the *rms* temperature difference (Fig. 15). In agreement with the above said, C1 does slightly better than C2, but a considerable improvement of the predicted temperature is provided by C3.

In the entire vertical range below about $2\,\mathrm{m}$, ΔT_{C3} is up to $0.2\,\mathrm{K}$ less than ΔT_{C1}. Only right at the surface, ΔT_{C3} is about $0.1\,\mathrm{K}$ higher than the corresponding value from C1 which is obviously due to the above mentioned mismatch after 15 June. Hence, C3 provides the best results for the temperature stratification in the thermocline. As the temperature in this depth range was definitely not affected by the heat exchange at the sea surface ($\approx 90\%$ of the short-wave radiation is absorbed in the uppermost $1\,\mathrm{m}$ depth range), its improvement could only be achieved by lateral advection which is controlled by the wind; apparently, the wind is better represented in the observations than in the weather forecasts. Summarised, the objective skill measure ΔT for the near-surface temperature and ΔD for the mixed-layer depths indicate that C1 provides the best forecast, while ΔT_{C3} is clearly superior to ΔT_{C1} and ΔT_{C2} in the thermocline.

The decision whether C1 or C3 will serve as control run in the subsequent series is facilitated by Fig. 16: qualitatively, the evolution of the predicted temperature pattern in C3 (Fig. 16c) resembles the observations (Fig. 16a) much better than in C1 (Fig. 16b). Namely, the near surface temperature is too high but the thickness of the warm layer 16–20 June is roughly the same as in the observations, close to $10\,\mathrm{m}$. Moreover, the depth and the variability of the maximum vertical temperature gradient in C3 resembles to a larger degree the observed pattern (compare Fig. 16d, e, f) but the vertical temperature gradients are still too weak. Hence, because of these qualitative criteria, C3 will be used as control run in Series D.

4.4 Series D: sensitivity to the vertical mixing parameterisation

The GLS scheme (Umlauf and Burchard, 2003) provides a generalisation of a class of differential length-scale equations used in turbulence models for oceanic flows. Commonly used models, like the $k - kl$ model of Mellor and Yamada (1982), the $k - \epsilon$ model (Rodi, 1987), and the $k - \omega$ model (Wilcox, 1988) are recovered as special cases of the generic scheme. Here, k is the turbulent kinetic energy, l the length scale of the turbulence, ϵ the dissipation rate, and ω the specific dissipation rate. In Series A–C, the GLS vertical mixing scheme was applied using its generic parameters as formulated by Umlauf and Burchard (2003). In the following, D1 is identical to C3, serving as control run, in D2 is applied the GLS scheme with the $k - l$ parameterisation, in D3 the $k - \epsilon$ parameters, and finally in D4 the $k - \omega$ parameterisation which was adjusted to oceanic conditions by Umlauf et al. (2003).

After 12 June, the near-surface temperature of all runs is to some degree correlated with the observations (Fig. 17a), but mostly it is still too high. Moreover, the graphs indicate that the temperatures from D2, D3, D4 are closer to the observed ones which is also expressed by $\Delta T \leq 0.6\,\mathrm{K}$ while $\Delta T = 0.78\,\mathrm{K}$ for D1. For the mixed-layer depth (Fig. 17b), the best agreement with the observations was obtained from D2 and D3 with $\Delta D_{C2} = 2.63\,\mathrm{m}$ and $\Delta D_{C2} = 2.72\,\mathrm{m}$, respectively. However, the mixed-layer was mostly to shallow. The final decision which mixing scheme performs best is supported by the vertical structure of ΔT displayed in Fig. 18. There is clear evidence that the $k - kl$ scheme (D2), the $k - \epsilon$ scheme (D3) and the $k - \omega$ scheme (D4) do better than the generic GLS (D1), but the best performance is obtained from D3 which is superior in the entire vertical range below about $2\,\mathrm{m}$ depth. Thus, D3 served as the control run in Series E.

4.5 Series E: sensitivity to the background vertical eddy diffusivity

The shortcoming of all model runs conducted so far was that the mixed-layer was too warm and too shallow. Hence, it was speculated the vertical transport of heat and momentum was not adequate. Several attempts were undertaken to fine-tune the D3 results by varying the vertical eddy viscosity coefficient and the turbulent closure parameters, but the outcomes were sobering – a significant improvement of the forecast skills for the mixed-layer properties was not achieved. Hence, in this series, the background vertical eddy diffusivity A_{VT} was increased gradually from $1 \times 10^{-6}\,\mathrm{m^2\,s^{-1}}$ in E1 (which is the control run identical to D3) to $2 \times 10^{-4}\,\mathrm{m^2\,s^{-1}}$ in E14. The forecast skill of each run was again assessed by means of ΔT at 0.81 m depth, and by ΔD. The dependency of these parameters on A_{VT} are shown in Fig. 19. ΔT exhibits a pronounced minimum of $\approx$ 0.52 K (0.08 K lower than in D3) for $A_{VT} = 1.5 \times 10^{-5}\,\mathrm{m^2\,s^{-1}}$ in E4, which is in close agreement with $(1.7 \pm 0.2) \times 10^{-5}\,\mathrm{m^2\,s^{-1}}$ obtained from tracer measurements in the thermocline during the North Atlantic Tracer Release Experiment (Thorpe, 2007). By contrast, the minimum of $\Delta D = 1.77$ m is found in E11 for $A_{VT} = 8 \times 10^{-5}\,\mathrm{m^2\,s^{-1}}$. In Fig. 20 are shown the near-surface temperature in E4 and the mixed-layer depth in E11, together with the corresponding quantities of the control run E1 and the observations. After 12 June, the increase of A_{VT} from $1 \times 10^{-6}\,\mathrm{m^2\,s^{-1}}$ to $1.5 \times 10^{-5}\,\mathrm{m^2\,s^{-1}}$ shifted the near-surface temperature by about 0.1 K closer to the observations. For most of the time, the modelled signal is clearly correlated with the observations, although the modelled maximum and minimum temperatures are frequently lagged a few hours behind the observed extreme values. This reason for this behaviour is unknown. For the mixed-layer depth, the increase of the eddy diffusivity to $8 \times 10^{-4}\,\mathrm{m^2\,s^{-1}}$ caused a significant reduction of ΔD from 2.72 m in E1 to 1.77 m in E11. While in the precursor series the mixed-layer was always too shallow, it agrees now remarkably well with the observations, except for a large discrepancy on 19 June where the predicted mixed-layer depth is underestimated by about 4 m.

5 Temporal variability

In order to assess the modelled temporal variability of the temperature and the depth of the mixed-layer, the spectrum of the near-surface temperature amplitude $\hat{T}$ at 0.81 m depth and the spectrum of the mixed-layer depth amplitude $\hat{D}$ were evaluated both from the observations and the ROMS outputs of runs E4 and E11, respectively. At first glance, the modelled spectrum of the near-surface temperature (Fig. 21a1) resembles the observations in the cycle period range between about 0.1 and 1 days but significant differences are evident in the bands between about 0.1 and 0.4 days where the modelled amplitude is partly up to one order of magnitude different from the observed one. This mismatch is not surprising, because here the temporal variability is controlled mainly by internal waves which are not or only partially reproduced by the model. By contrast, the 0.4–0.7 days band (10–17 hr) is the range dominated by tides and inertial motions. Theoretically at 40°N, the inertial peak is at 18.7 hr (0.78 days), but a corresponding small peak is only visible in the modelled spectrum. No such peak is noticeable in the observations. Probably, it is obscured by the neighbouring longer cycle periods (the periods resolved in this band are 17.1, 18.7, and 20.5 hr). Additional peaks are found at about 0.4 days (10 hr) and 0.6 days (14 hr) which might be related to a semi-diurnal tidal component. As there was no tidal forcing in the ROMS version utilised in this study, and the MERCATOR forcing at the lateral boundaries was defined by means of daily averages, the semi-diurnal variability is probably caused by

tides of the atmosphere. Both the modelled and the observed spectrum are dominated by the diurnal variability, represented by the peak at 1.0 days. In the red part of the spectrum between 1 and about 4 days, the modelled amplitude $\hat{T}_{ROMS}$ is always higher than the observed amplitude $\hat{T}_{obs}$, and for periods longer than 4 days, the observed amplitudes are higher. The author refrains from discussing this matter which is potentially impacted by long-period fluctuations of the forcing at the surface

5 and at the lateral boundaries. More detailed information of the correlation $r_{\hat{T}_{ROMS},\hat{T}_{obs}}$ between the modelled and observed temperature amplitudes is gained from Fig. 21a2: the correlation coefficient $r = 0.81$ together with the p-value $p = 1.09 \times 10^{-15}$ proves a high significant correlation, and the regression coefficients $a_0 = 0.04, a_1 = 0.74$ indicate that in general the modelled amplitudes are somewhat underestimated. By contrast, there is only a low correlation between the modelled and the observed mixed-layer amplitudes $\hat{D}_{ROMS}$ and $\hat{D}_{obs}$, respectively (Fig. 21b2), which is indicated by $r_{\hat{D}_{ROMS},\hat{D}_{obs}} = 0.40$. And the rather

10 high value $p = 1.40 \times 10^{-4}$ shows that the correlation is to a lesser extent significant. This finding is also supported by the spectrum (Fig. 21b2). Here, a slight agreement of the amplitudes is only found for the diurnal cycle.

6   Horizontal variability

In order to assess the capability of ROMS to reproduce and predict the horizontal variability of mixed-layer properties, the results of Run E7 were analysed along the ScanFish tracks A03, A05, A07, A09, and A10 (see Fig. 4), and compared with the

15 data collected by the towed device. E7, using $A_{VT} = 4 \times 10^{-5}\,\mathrm{m^2\,s^{-1}}$, was selected for this comparison because both ΔT and ΔD were acceptable. Details of the ScanFish tracks are summarised in Table 2. As ROMS output was only available in 6-hr intervals starting at midnight, in each case that output cycle was used which fell within the time window when the tracks were conducted. This assumed synopticity of the ScanFish tracks which is justified by the fact that the maximum duration of the tracks was 5 hr 28 minutes for A03.

20   To make the ScanFish observations and the ROMS products comparable, the ScanFish temperature was interpolated vertically on 1-dbar standard levels and the ROMS temperature was mapped on the same levels. As the upper inflection point of the ScanFish varied between about 5 and 10 dbars, there was frequently no information on the near-surface temperature available. In such cases, the temperature at the inflection level was extended to the surface. The same method was applied to the ROMS temperature which is not defined right at the surface but at the first s-level below the surface. In deep-water regions, this level

25 is located at about 7.5 m depth.

    In Fig. 22a is shown a temperature section from the ScanFish measurements along the central track A05, and the corresponding section from ROMS is displayed in Fig. 22b. The gross features of both sections resemble each other, but the small-scale horizontal variability of the Scanfish temperature was not reproduced by ROMS. This is probably due to the smoothing effect of the OA or due to the combined action of the horizontal eddy diffusivity and numerical diffusion. However, as the last as-

30 similation cycle was conducted on 12 June 10 days prior to the ScanFish observations, one may exclude that the OA removed the small scale features. Moreover, the vertical temperature gradient is much weaker in ROMS which was already noticed in the C-Series above. Hence, this is apparently not caused by the increased vertical diffusivity but by the vertical resolution of ROMS. The near-sea surface temperatures and the mixed-layer depths from the ScanFish and ROMS are displayed in Figs.

22c and 22d. The modelled and the observed quantities are rather similar and also the large-scale variabilities agree rather well. Maximum differences between the sea surface temperatures are close to 0.5 K, and the maximum difference between the modelled and the observed mixed-layer depth is around 4 m at 14 km distance. Otherwise, the predicted mixed-layer depth reproduced almost perfectly the observed one. However, as noticed already above, the smaller-scale $\mathcal{O}(1\,\mathrm{km})$ observed variability

5 was not reproduced by ROMS.

To investigate why the small-scale variability was not predicted correctly, Run E7 was repeated but now using a smaller horizontal eddy diffusivity coefficient of $1\,\mathrm{m}^2\,\mathrm{s}^{-1}$ instead of $10\,\mathrm{m}^2\,\mathrm{s}^{-1}$ which was used for all model runs so far. The reduced diffusivity actually amplified the predicted variability but this was scarcely correlated with the observations. Probably, a large fraction of the modelled variability was just 2-Δx noise. Thus, one has to settle for the fact that the present setup of ROMS is

10 only able to reproduce the horizontal variability of mixed-layer properties on those scales which are comparable to the Rossby radius.

7 Conclusions

ROMS has been utilised to diagnose and predict properties of the ocean mixed-layer, and the sensitivity of the model results to the choice of the initial and boundary conditions and vertical mixing schemes was investigated. The initial and lateral boundary

15 conditions for ROMS were taken from two different parent models by one-way nesting. At the surface, ROMS was forced by different weather forecasts, or by observations. All ROMS nowcasts and forecasts were validated against observations which were taken in June 2014 to the west of Sardinia in the Mediterranean Sea.

To explore the sensitivity of the near-surface temperature and the mixed-layer depth to the choice of the initial conditions, ROMS was alternatively initialised by MFS and MERCATOR, and in addition, observed temperature and salinity data were

20 assimilated. For validation, time series of temperature were compared with observed time series from a mooring. Initialising ROMS from MERCATOR instead of MFS provided a better agreement between the model and the observations, but a significant improvement was obtained from a ROMS run initialised from MERCATOR and updated with assimilated data from CTD casts and gliders. This applies both to the near-surface temperature, the mixed-layer depth, and as well to the temperature distribution in the upper thermocline.

25 To investigate the impact of the surface boundary conditions, atmospheric forcing fields were taken from the weather prediction models COSMO-ME and COSMO-IT, and from observations of a meteorological buoy acting as a point source. With respect to the mixed-layer depth, the best agreement with the observations was obtained from a model run forced with COSMO-ME, while the near-surface temperature exhibited the best match when ROMS was forced by either of the two weather prediction models. However, the stratification in the upper thermocline was best represented when the point source was applied. The

30 obvious reason for this surprising result is that the momentum forcing was overestimated by both COSMO-ME and COSMO-IT.

For the vertical mixing, four different configurations of the GLS scheme of Umlauf and Burchard (2003) were applied, representing the generic version, the $k - kl$ model of Mellor and Yamada (1982), the $k - \epsilon$ model (Rodi, 1987), and the $k - \omega$ model (Wilcox, 1988). The best performance was obtained from the $k - \epsilon$ model.

Regardless of which initial conditions or surface boundary conditions were applied – the modelled mixed-layer was always

5 to shallow and too warm. Therefore, the background vertical eddy diffusivity coefficient A_{VT} was varied over more than one order of magnitude. The best agreement of the mixed-layer temperature was obtained for $A_{VT} = 1.5 \times 10^{-5}\,\mathrm{m^2\,s^{-1}}$ while $A_{VT} = 8 \times 10^{-5}\,\mathrm{m^2\,s^{-1}}$ provided the best match of the mixed-layer depth with the observations.

A positive and significant correlation was found between the modelled and the observed temporal variability of the mixed-layer temperature. The modelled variability resembled the observed variability predominantly for cycle periods in the spectral

10 ranges between about 0.1 and 1 days. By contrast, less correlation was found between the modelled and the observed variability of the mixed-layer depth. A slight agreement was only found for the diurnal period.

The horizontal variability was validated against measurements from a high-resolution zonal ScanFish section. Both the modelled mixed-layer temperature and the mixed-layer depth closely resembled the observations, but only on the larger scales of $\mathcal{O}(10\,\mathrm{km})$. Hence, the mesoscale variability was rather well reproduced but the sub-mesocale variability was not.

15 **Code availability**

All work related to this article was done on a Linux workstation under Kubuntu 16.04. ROMS/TOMS version 3.6 was used for the model runs, the pre- and postprocessing was done with MATLAB R2016b, and the article was written in LaTeX. The model code and all scripts are available from the author on request.

Data availability

20 All data of the REP14-MED experiment are available on the CMRE data server at `http://geos3.cmre.nato.int`. The data are NATO UNCLASSIFIED and available only for the partners of the experiment. However, interested institutions can sign up for partnership at any time. Requests may be directed to the author or to <geos-webmaster@nurc.nato.int>.

Competing interests

The author declares that he has no conflict of interest.

25 *Acknowledgements.* The author would like to thank the masters and crews of NRV *Alliance* and RV *Planet* for their professionalism during the conduction of the experiments at sea. The data from COSMO-ME and COSMO-IT were provided by the Italian weather service *Centro Nazionale di Meteorologia e Climatologia Aeronautica.* REP14-MED was sponsored by *HQ Supreme Allied Command Transformation* (Norfolk, VA, USA).

References

Bretherton, F.P., R.E. Davies, and C.B. Fandry (1976) Technique for Objective Analysis and design of oceanographic experiments applied to Mode-73. *Deep-Sea Research*, **23**, 559–582.

Carter, E.F., and A.R. Robinson (1987) Analysis models for the estimation of oceanic fields. *Journal of Atmospheric and Oceanic Technology*, **4**, 49–74.

Chapman, D. C. (1985) Numerical treatment of cross-shelf open boundaries in a barotropic coastal ocean model. *Journal of Physical Oceanography*, **15**, 1060–1075.

Chen C.T., and F.J. Millero (1977) Speed of sound in seawater at high pressures. *Journal of the Acoustic Society of America*, **62**(5), 1129–1135.

Dietrich, G., Kalle, K., Krauss, W., and G. Siedler (1975) Allgemeine Meereskunde. Gebrüder Bornträger, 593pp.

Dombrowsky E., L. Bertino, G.B. Brassington, E.P. Chassignet, F. Davidson, H.E. Hurlburt, M. Kamachi, T. Lee, M.J. Martin, S. Meu, and M. Tonani (2009): GODAE Systems in Operation, *Oceanography*, **22**, 3, 83–95.

Drévillon, M., R. Bourdallé-Badie, C. Derval, J.M. Lellouche, E. Rémy, B. Tranchant, M. Benkiran, E. Greiner, S. Guinehut, N. Verbrugge, G. Garric, C.E. Testut, M. Laborie, L. Nouel, P. Bahurel, C. Bricaud, L. Crosnier, E. Dombrowsky, E. Durand, N. Ferry, F. Hernandez, O. Le Galloudec, F. Messal, and L. Parent (2008) The GODAE/Mercator-Ocean global ocean forecasting system: results, applications and prospects, *Journal of Operational Oceanography*, **1**, 1, 51–57, DOI: 10.1080/1755876X.2008.11020095.

Fairall, C.W., E.F. Bradley, D.P. Rogers, J.B. Edson, and G.S. Young (1996) Bulk parameterization of air-sea fluxes for Tropical Ocean-Global Atmosphere Coupled-Ocean Atmosphere Response Experiment, *Journal of Geophysical Research*, **101**(C2), 3747–3764, DOI: 10.1029/95JC03205.

Grilli, F., and N. Pinardi (1998) The computation of Rossby radii of deformation for the Mediterranean Sea. *MTP news*, **6**, 4.

Katsnelson, B., Petnikov, V., and J. Lynch (2012) Fundamentals of Shallow Water Acoustics. DOI: 10.1007/978-1-4419-9777-7, Springer, 540pp.

Lurton, X. (2010) An Introduction to Underwater Acoustics. DOI: 10.1007/978-3-642-13835-5, Springer, 680pp.

Marchesiello, P., McWilliams, J. C., and A. F. Shchepetkin (2001) Open boundary conditions for long-term integration of regional ocean models. *Ocean Modelling*, **3**, 1–20.

Mellor, G.L. and T. Yamada (1982) Development of a turbulence closure model for geophysical fluid problems. *Reviews of Geophysics and Space Physics*, **20**, 851–875.

Medwin, H., and C.S. Clay (1998) Fundamentals of Acoustic Oceanography. Academic Press, 712pp.

Onken, R., M. Ampolo-Rella, G. Baldasserini, I. Borrione, D. Cecchi, E. Coelho, S. Falchetti, H.-V. Fiekas, A. Funk, Y.-M. Jiang, M. Knoll, C. Lewis, B. Mourre, P. Nielsen, A. Russo, and R. Stoner (2014) REP14-MED Cruise Report, CMRE-CR-2014-06-REP14-MED, CMRE, La Spezia, 76 pp.

Onken, R., H.-V. Fiekas, L. Beguery, I. Borrione, A. Funk, M. Hemming, K. J. Heywood, J. Kaiser, M. Knoll, P.-M. Poulain, B. Queste, A. Russo, K. Shitashima, M. Siderius, and E. Thorp Küsel (2016) High-Resolution Observations in the Western Mediterranean Sea: The REP14-MED Experiment. *Ocean Science* (submitted).

Pace, N.G., and F.B. Jensen (Eds.) (2002) Impact of Littoral Environmental Variability on Acoustic Predictions and Sonar Performance. Kluwer Academic, 620pp.

Rodi, W. (1987) Examples of calculation methods for flow and mixing in stratified fluids. *Journal of Geophysical Research*, **92**, (C5), 5305–5328.

Shchepetkin, A. F., and J. C. McWilliams (2003) A method for computing horizontal pressure gradient force in an oceanic model with a nonaligned vertical coordinate, *Journal of Geophysical Research*, **108**(C3), 3090, DOI: 10.1029/2001JC001047.

5 Shchepetkin, A. F., and J. C. McWilliams (2005) The Regional Ocean Modeling System: A split-explicit, free-surface, topography following coordinates ocean model, *Ocean Modelling*, **9**, 347–404.

Song, Y. and D. B. Haidvogel (1994) A semi-implicit ocean circulation model using a generalized topography-following coordinate system. *Journal of Computational Physics*, **115**(1), 228–244.

Thorpe, S. A. (2007) An Introduction to Ocean Turbulence. Cambridge University Press, 293pp.

10 Tonani M., A. Teruzzi, G. Korres, N. Pinardi, A. Crise, M. Adani, P. Oddo, S. Dobricic, C. Fratianni, M. Drudi, S. Salon, A. Grandi, G. Girardi, V. Lyubartsev and S. Marino (2014) The Mediterranean Monitoring and Forecasting Centre, a component of the MyOcean system. *Proceedings of the Sixth International Conference on EuroGOOS 4–6 October 2011, Sopot, Poland.* Edited by H. Dahlin, N.C. Fleming, and S.E. Petersson. EuroGOOS Publication no. 30, ISBN 978-91-974828-9-9.

Umlauf, L., and H. Burchard (2003) A generic length-scale equation for geophysical turbulence models. *Journal of Marine Research*, **61**, 15 235–265.

Umlauf, L., H. Burchard, an K. Hutter (2003) Extending the $k - \omega$ turbulence model towards oceanic applications. *Ocean Modeling*, **5**, 195–218.

Wilcox, D. C. (1988) Reasessment of the scale-determining equation for advanced turbulence models. *AIAA Journal*, **26**, 1299-1310.

Table 1. Nominal and actual depths of the Starmon and RBR sensors mounted on the appendix of mooring M1. For the meaning of the recorded variables see text.

sensor position	sensor type	recorded variables	nominal depth [m]	mean actual depth [m]	remarks
1	Starmon	t, T	0.0	0.81	
2	Starmon	t, T	0.5	1.30	
3	Starmon	t, T	1.0	1.79	
4	Starmon	t, T	1.5	2.28	
5	Starmon	t, T	2.0	2.77	
6	Starmon	t, T	2.5	3.26	
7	Starmon	t, T	3.0	3.76	failed after 9 June 19:39
8	Starmon	t, T	3.5	4.25	
9	Starmon	t, T	4.0	4.74	
10	Starmon	t, T	4.5	5.23	
11	Starmon	t, T	5.0	5.72	
12	Starmon	t, T	5.5	6.23	
13	Starmon	t, T	6.0	6.71	
14	Starmon	t, T	6.5	7.21	
15	Starmon	t, T	7.0	7.70	broken
16	Starmon	t, T	7.5	8.19	
17	Starmon	t, T	8.0	8.69	
18	Starmon	t, T	8.5	9.18	
19	Starmon	t, T	9.0	9.68	
20	Starmon	t, T	9.5	10.17	
21	Starmon, RBR	t, T, p	10.0	10.69	
22	Starmon	t, T	11.0	11.66	
23	Starmon	t, T	12.0	12.65	
24	Starmon	t, T	13.0	13.65	
25	Starmon	t, T	14.0	14.64	
26	Starmon	t, T	15.0	15.63	
27	Starmon	t, T	16.0	16.63	
28	Starmon	t, T	17.0	17.63	
29	Starmon	t, T	18.0	18.63	
30	Starmon	t, T	19.0	19.62	
31	Starmon, RBR	t, T, p	20.0	20.63	
32	Starmon	t, T	22.0	22.63	
33	Starmon	t, T	24.0	24.64	
34	Starmon	t, T	26.0	26.65	
35	Starmon	t, T	28.0	28.67	
36	Starmon, RBR	t, T, p	30.0	30.69	
37	Starmon	t, T	32.0	32.71	
38	Starmon	t, T	34.0	34.74	
39	Starmon	t, T	36.0	36.77	
40	Starmon	t, T	38.0	38.81	
41	Starmon, RBR	t, T, p	40.0	40.85	

Table 2. Timing and nominal positions of ScanFish tracks considered in this study (cf. Fig. 4). *ROMS analysis* determines the instant of the model output which was used for comparison. *Only the strictly meridional fraction of A10 was utilised.

track	type	nominal position	start time	end time	duration	ROMS analysis
A01	zonal	40°06' N	21 June 14:03	21 June 18:15	4:12	21 June 18:00
A03	zonal	40°00' N	21 June 19:10	22 June 00:38	5:28	22 June 00:00
A05	zonal	39°48' N	22 June 03:00	22 June 08:00	5:00	22 June 06:00
A07	zonal	39°36' N	22 June 12:57	22 June 18:05	5:08	22 June 18:00
A09	zonal	39°24' N	22 June 20:17	23 June 01:16	4:59	23 June 00:00
A10*	meridional	07°31' E	23 June 18:20	23 June 22:15	3:55	24 June 00:0h
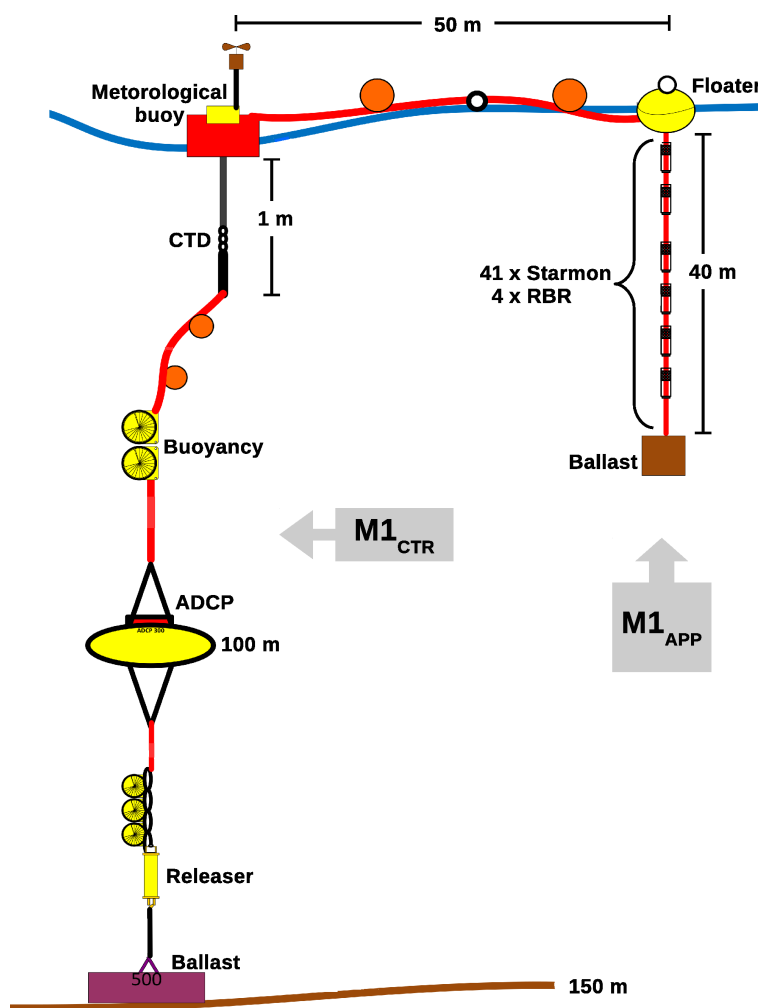
Figure 1. Design drawing of mooring $M1$. For explanations see text.
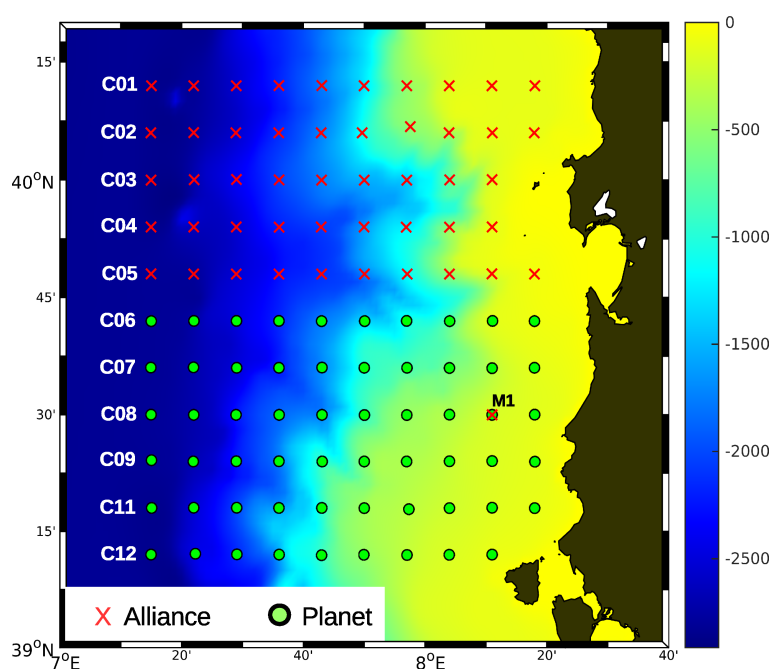
Figure 2. CTD casts taken by *Planet* and *Alliance* 7–11 June. Zonal CTD sections are labelled C01, ..., C12, the position of mooring M1 is indicated on section C08. The colourbar indicates the water depth [m].
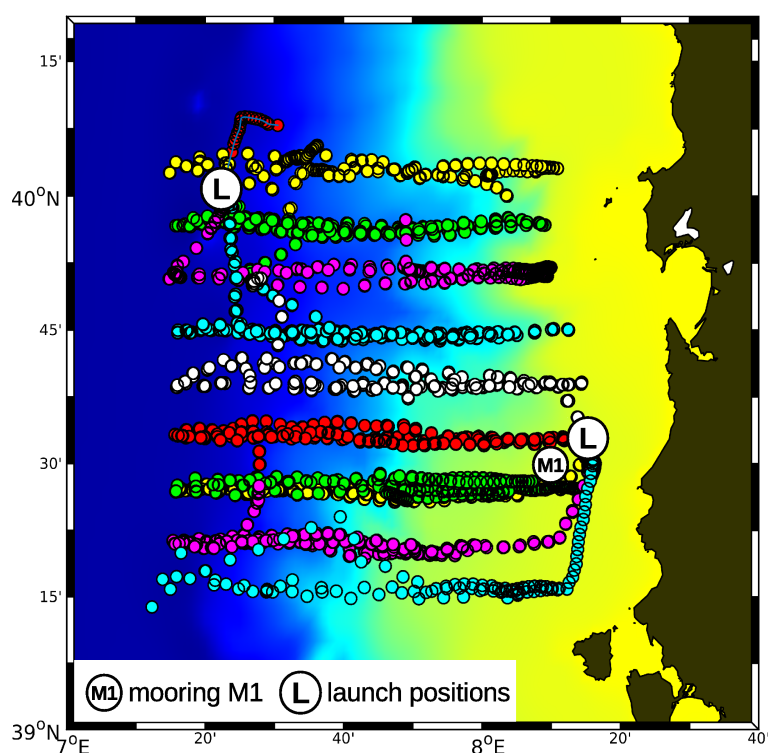
Figure 3. Actual tracks of gliders 8–23 June. The small dots along the tracks show the surfacing positions. Each glider is marked by a different colour. The colour code for the bathymetry is the same as in Fig. 2.
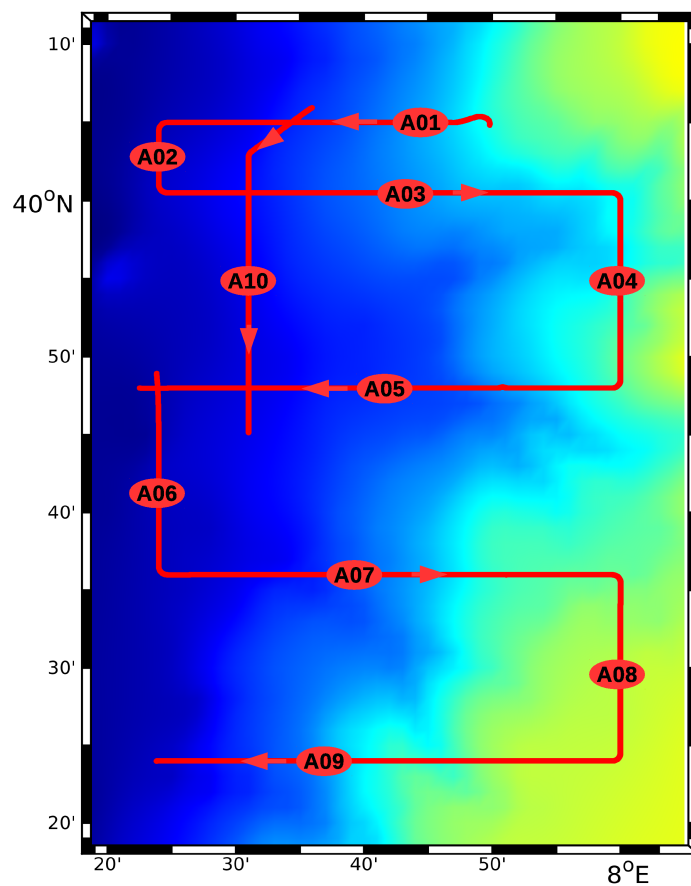
Figure 4. ScanFish tracks of *Alliance*, 21–24 June. The colour code for the bathymetry is the same as in Fig. 2
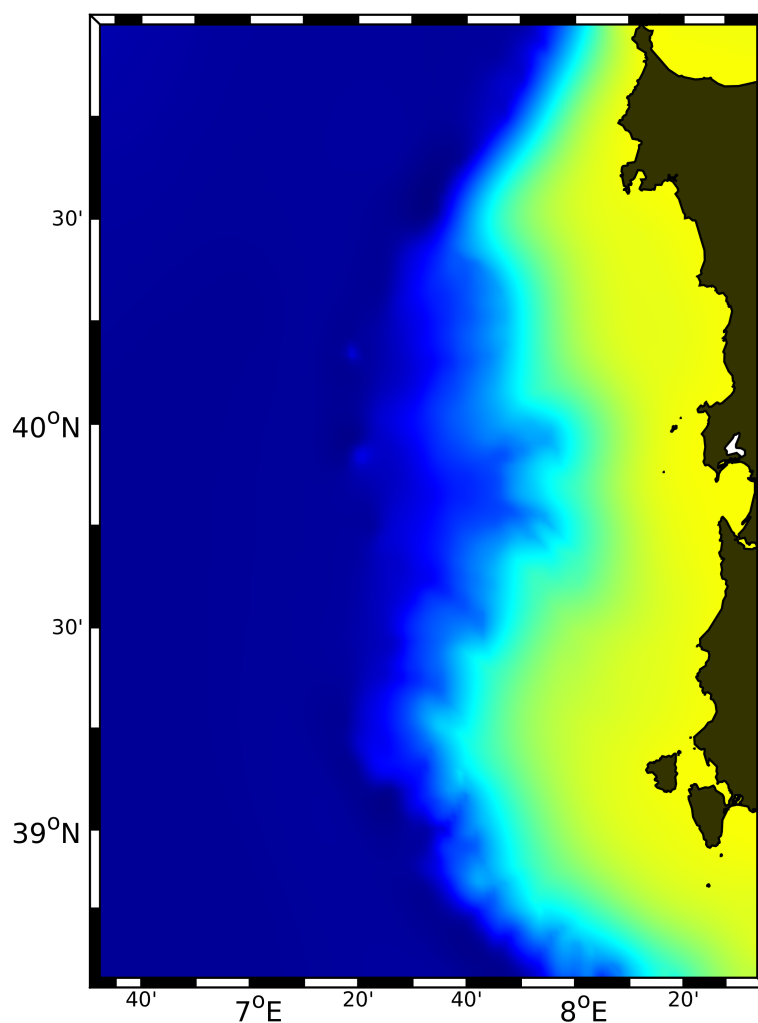
Figure 5. The model domain; the colour code for the bathymetry is the same as in Fig. 2 and indicates the water depth after smoothing.
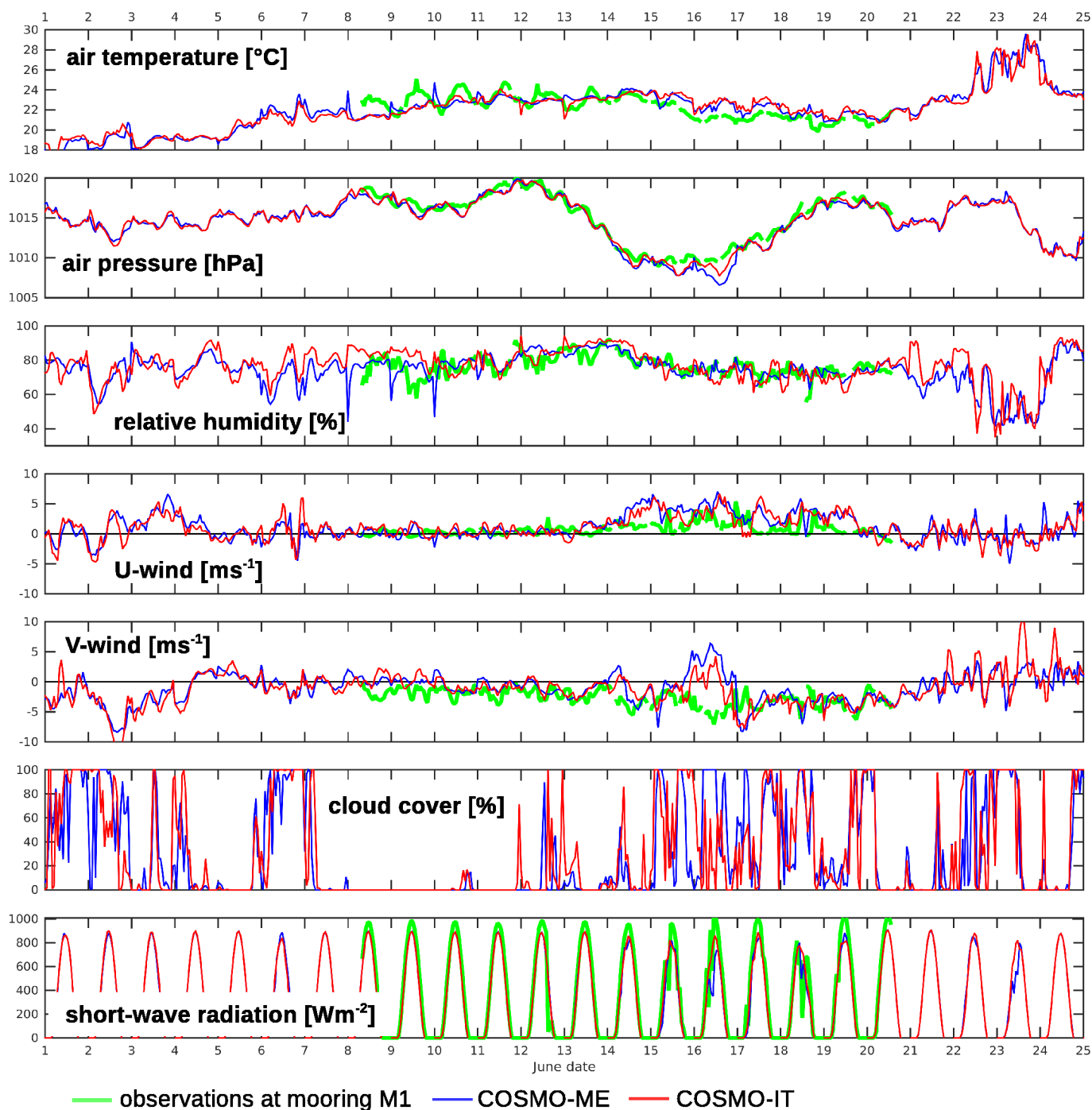
Figure 6. Time series of measured and predicted atmospheric parameters at the site of mooring M1 from observations of the meteorological buoy on top of M1, COSMO-ME, and COSMO-IT. *U-wind* and *V-wind* stand for the zonal and meridional wind components, respectively. The cloud cover was not recorded at M1. Precipitation is not shown, because no precipitation was predicted or measured during the entire period.
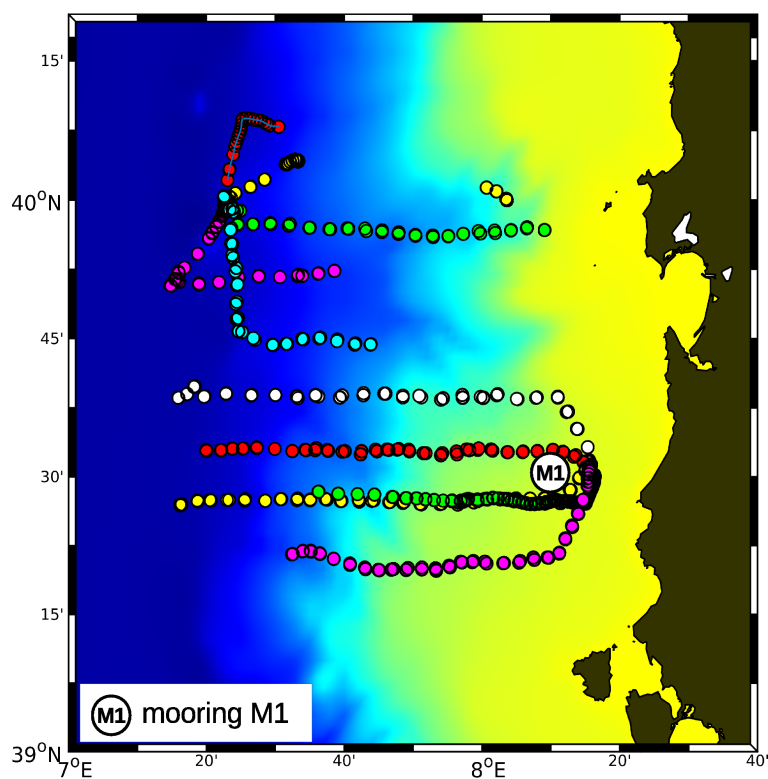
Figure 7. Actual surfacing positions of all assimilated gliders 7–12 June. Each glider is marked by a different colour. The colour code for the bathymetry is the same as in Fig. 2.
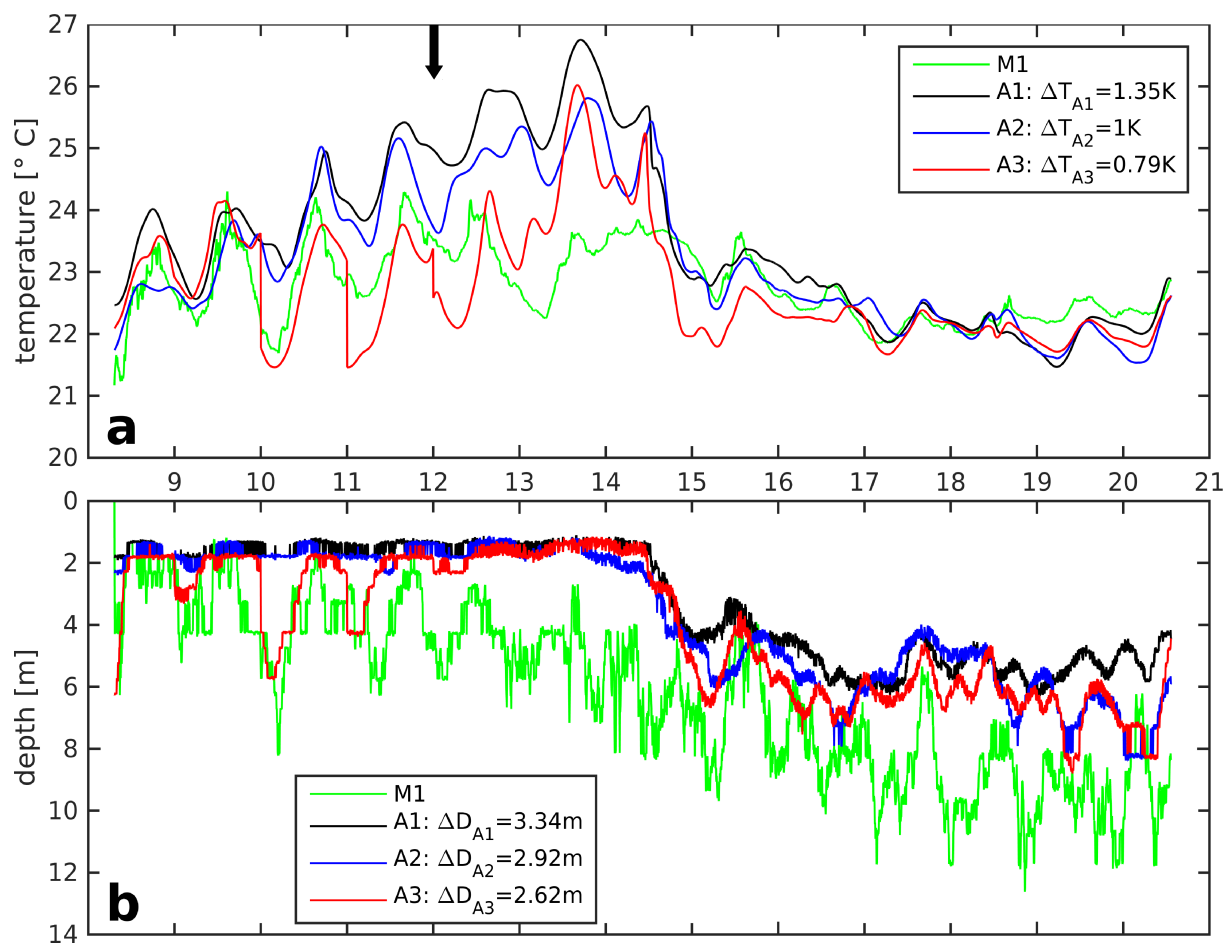
Figure 8. ROMS runs A1, A2, A3: time series of (a) near surface temperature at 0.81 m depth and (b) mixed-layer depth, and the corresponding observations at mooring M1. The numbers on the abscissae indicate June dates. The instant of the last assimilation is marked by the black arrow in (a).
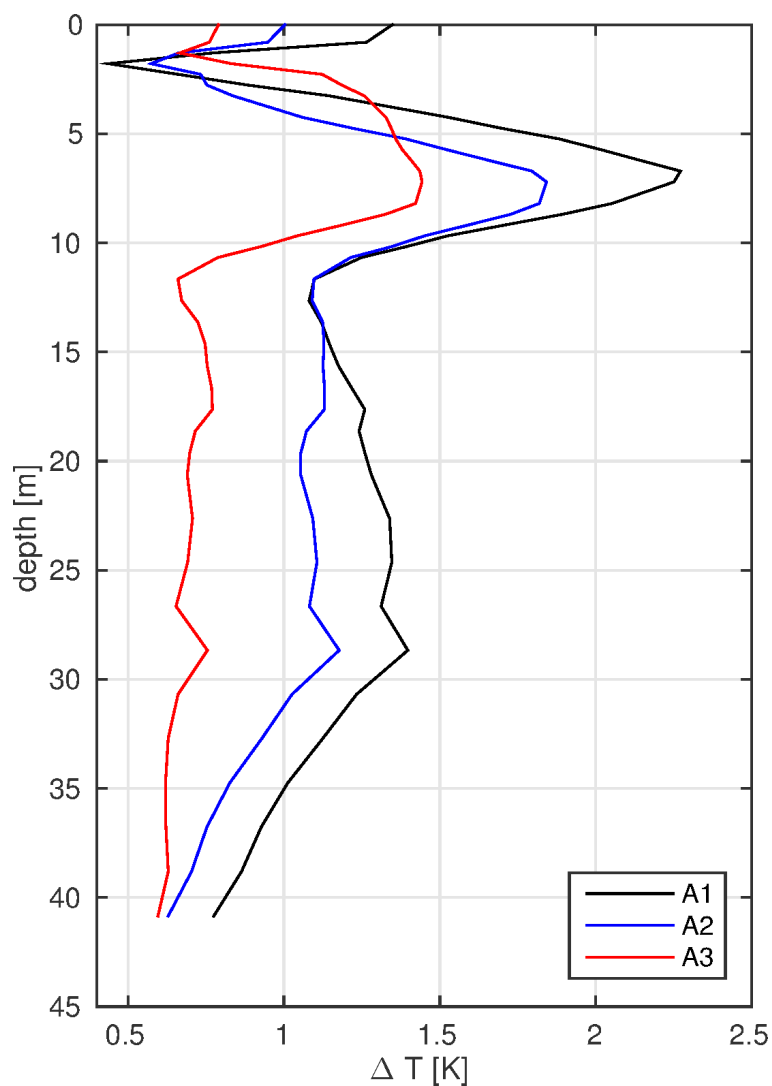
Figure 9. ROMS runs A1, A2, A3: *rms* temperature differences ΔT [K] between the modelled temperature T_{ROMS} and the observed temperature T_{obs}, evaluated at the actual depths of the observations. ΔT was computed only for the period of time after 12 June 00:00h.
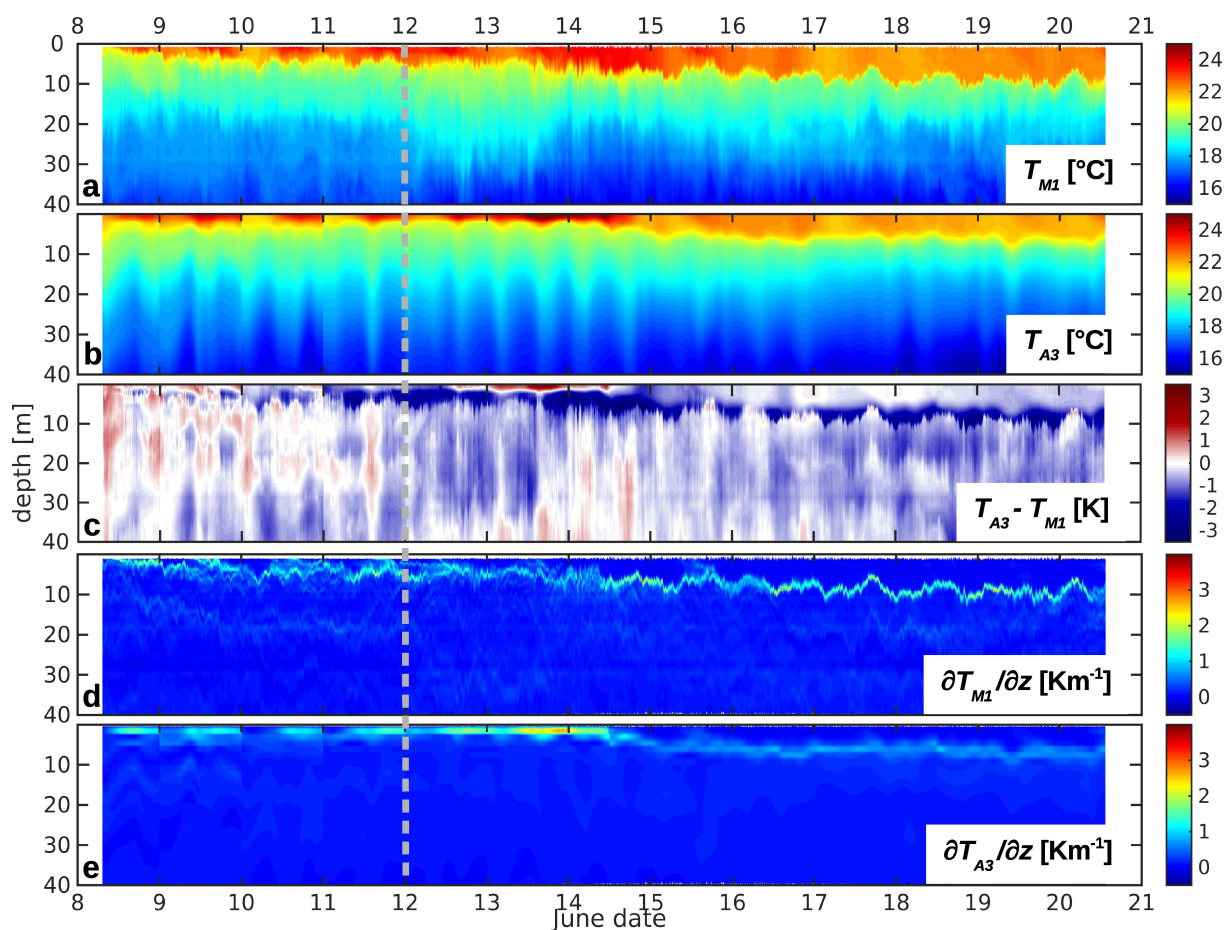
Figure 10. (a) Observed temperature at mooring M1, (b) modelled temperature from ROMS run A3, and (c) the difference between the modelled and the observed temperature. The vertical temperature gradient from (d) observations and (e) from A3. The instant of the last data assimilation is indicated by the the grey-dashed vertical line.
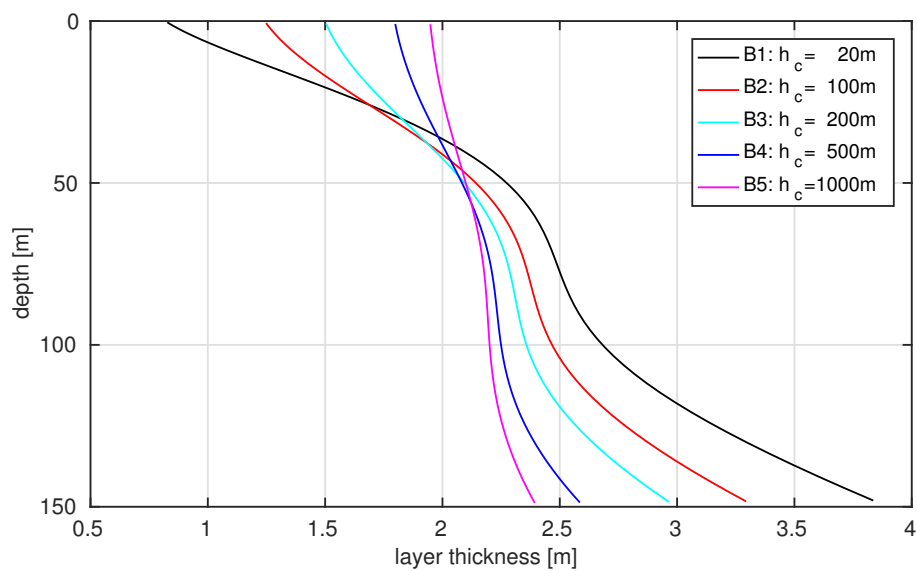
Figure 11. The layer thicknesses at the position of mooring M1 for various assumptions of the critical depth h_c
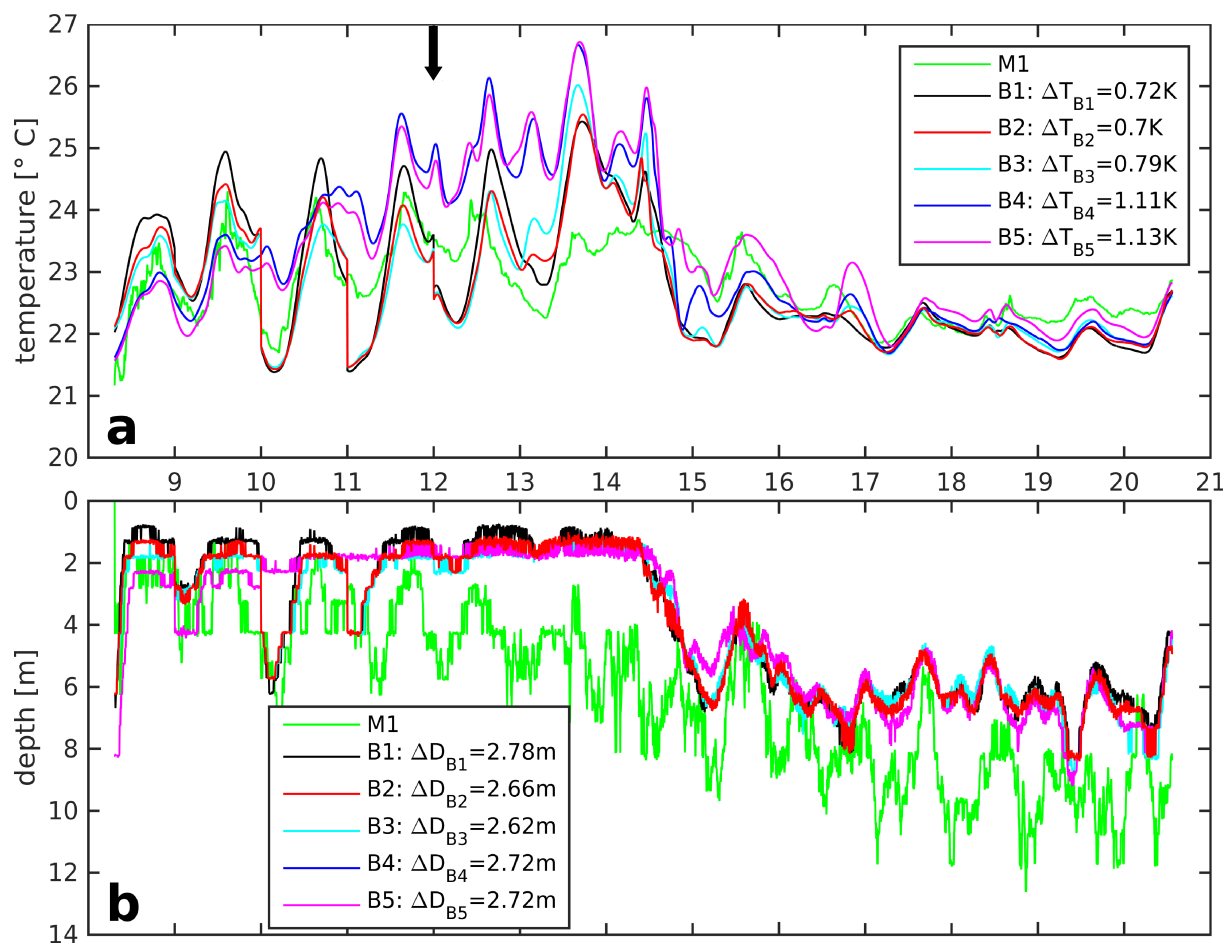
Figure 12. ROMS runs B1–B5: time series of (a) near surface temperature at 0.81 m depth and (b) mixed-layer depth, and the corresponding observations at mooring M1. The numbers on the abscissae indicate June dates. The instant of the last assimilation is marked by the black arrow in (a).
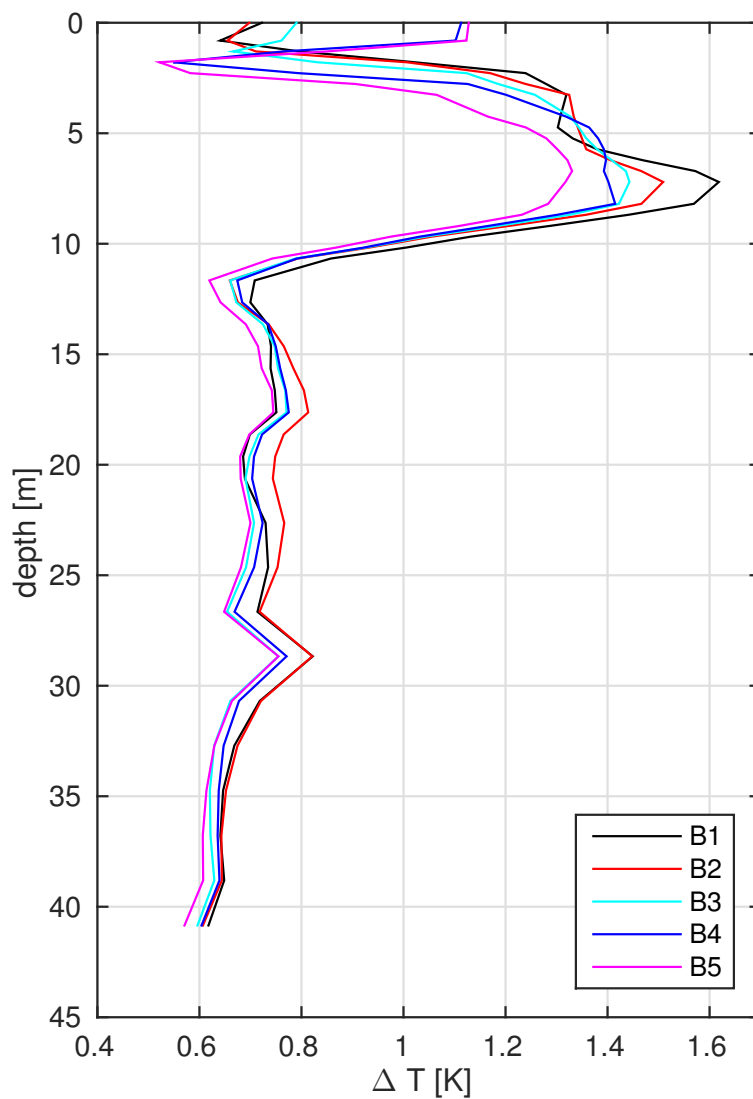
Figure 13. ROMS runs B1–B5: *rms* temperature differences ΔT [K] between the modelled temperature T_{ROMS} and the observed temperature T_{obs}, evaluated at the actual depths of the observations. ΔT was computed only for the period of time after 12 June 00:00h.
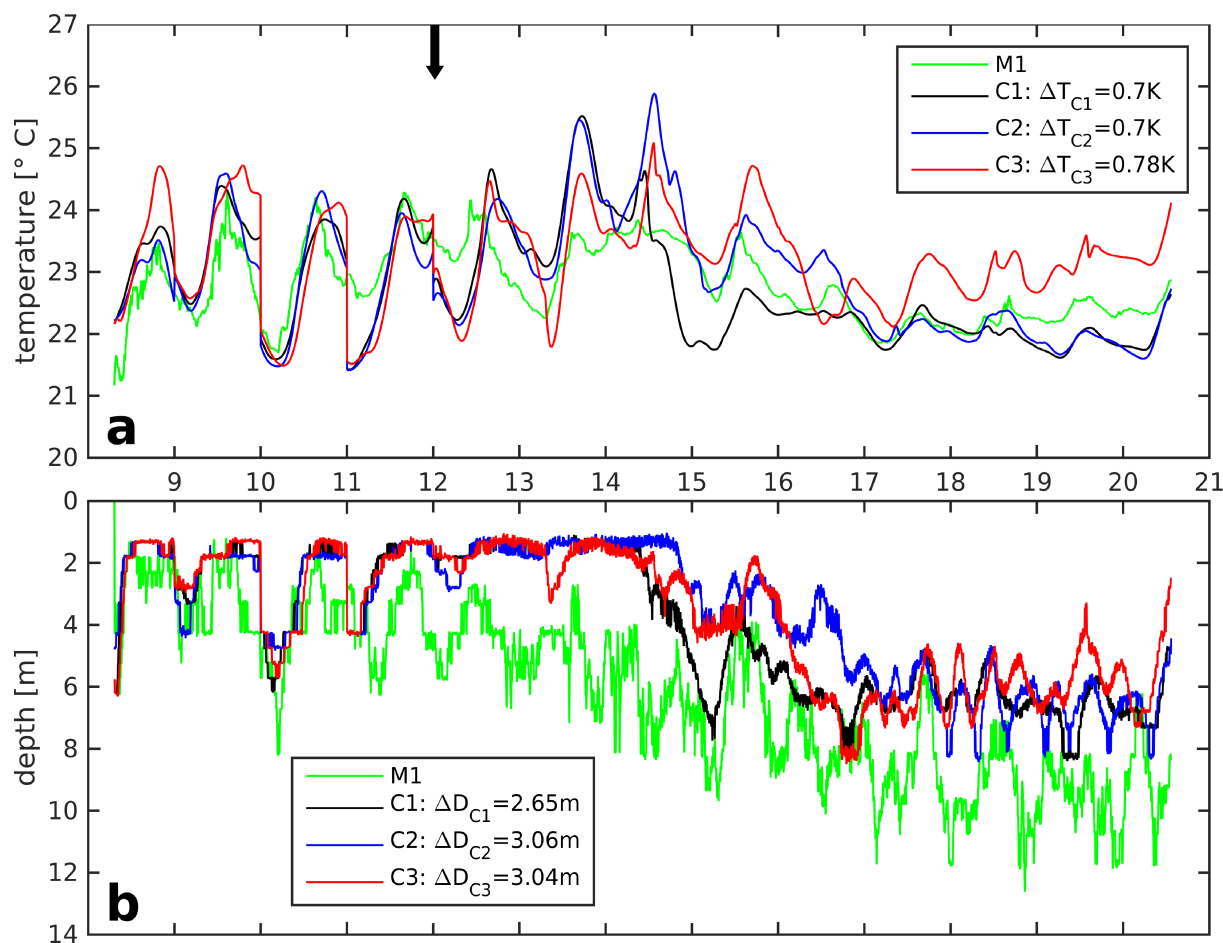
Figure 14. ROMS runs C1, C2, C3: time series of (a) near surface temperature at 0.81 m depth and (b) mixed-layer depth, and the corresponding observations at mooring M1. The numbers on the abscissae indicate June dates. The instant of the last assimilation is marked by the black arrow in (a).
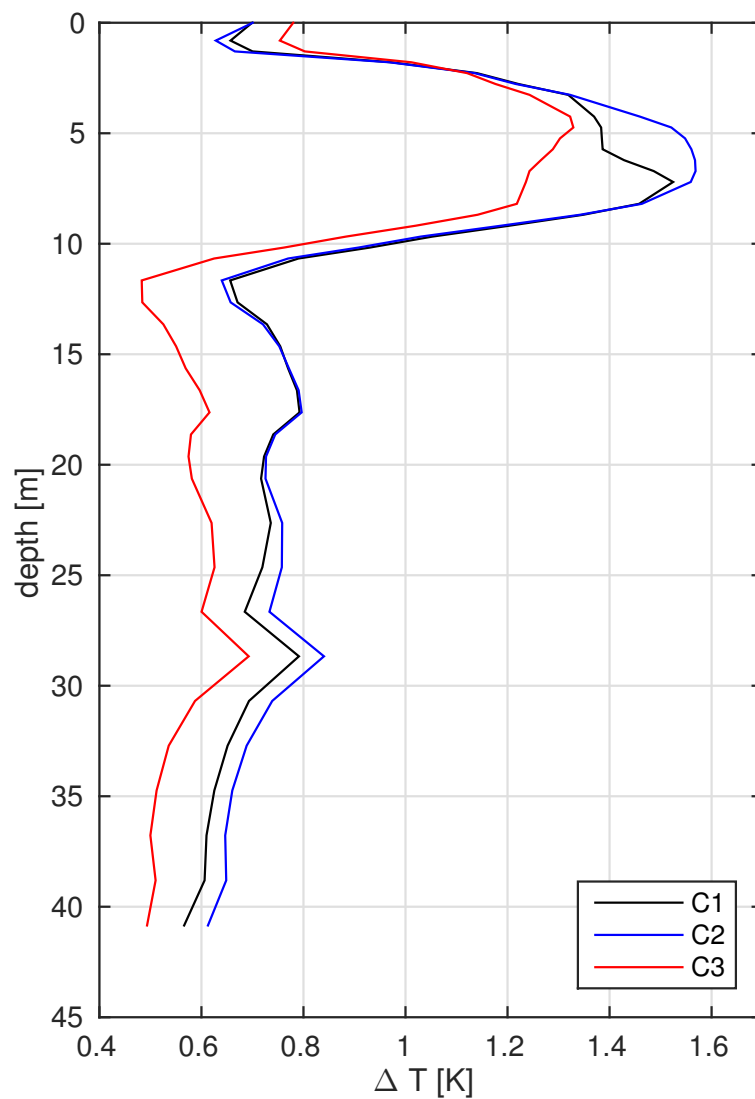
Figure 15. ROMS runs C1, C2, C3: *rms* temperature differences ΔT [K] between the modelled temperature T_{ROMS} and the observed temperature T_{obs}, evaluated at the actual depths of the observations. ΔT was computed only for the period of time after 12 June 00:00h.
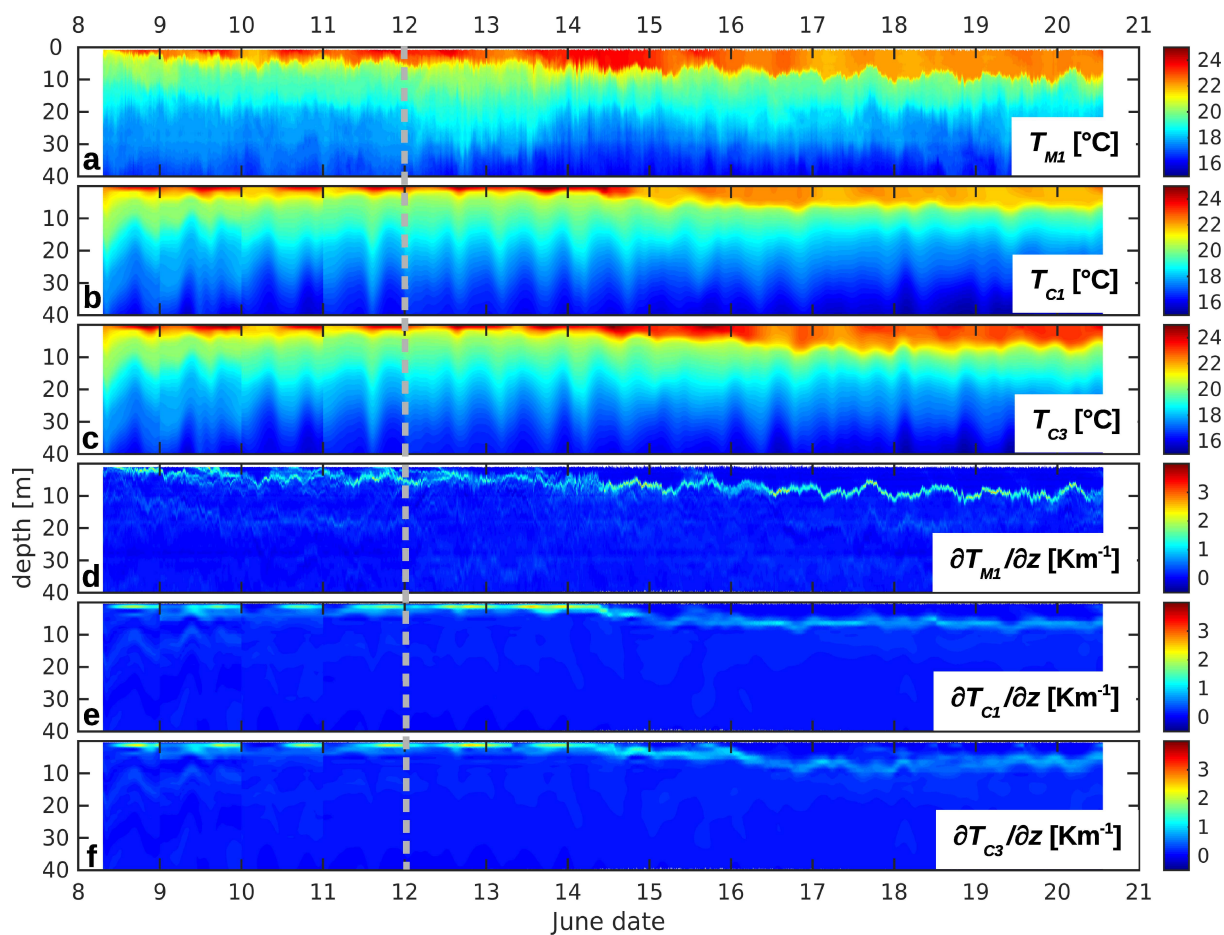
Figure 16. (a) Observed temperature at mooring M1, (b) modelled temperature from ROMS run C1 and (c) from C3, (d) the vertical temperature gradient from M1, (e) C1 and (f) C3. The instant of the last data assimilation is indicated by the the grey-dashed vertical line.
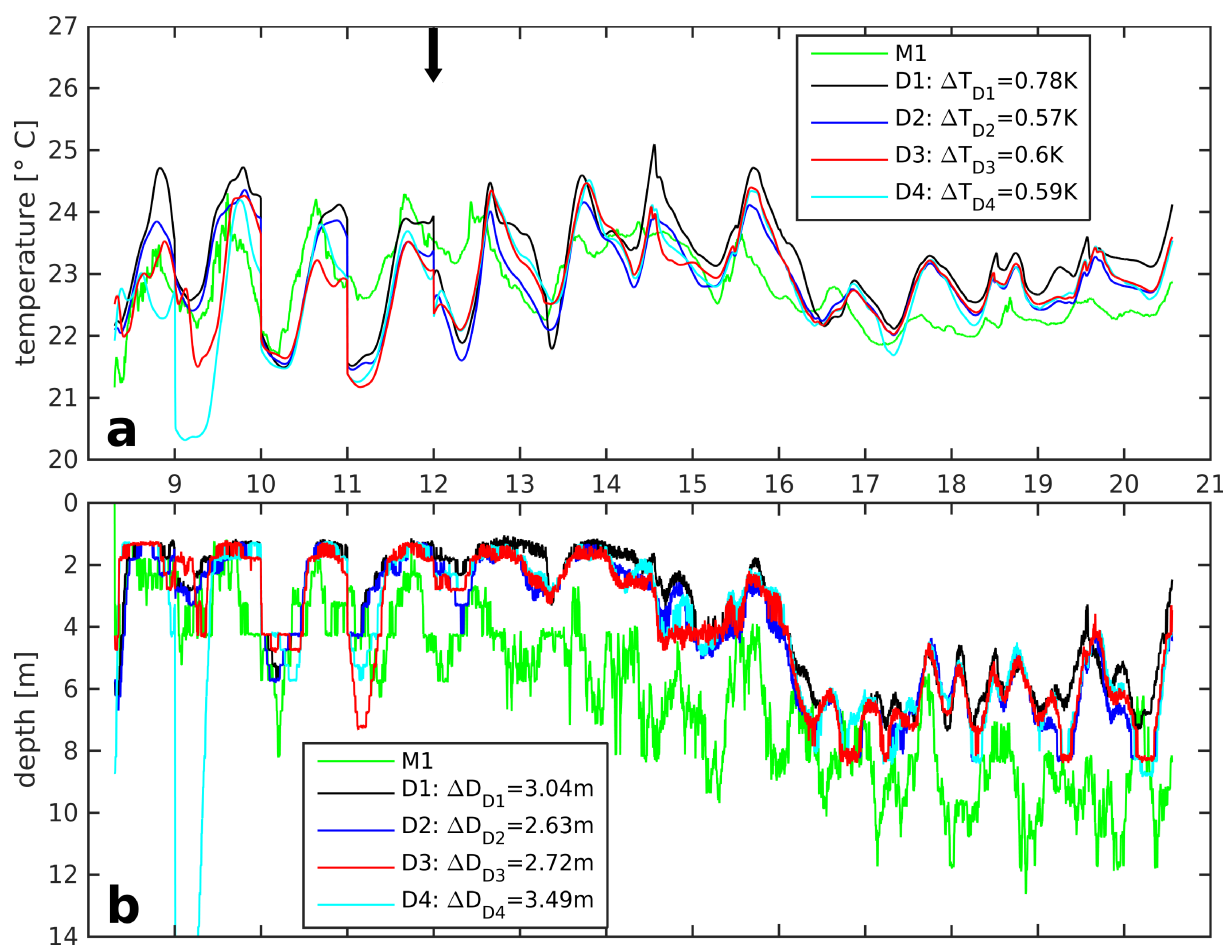
Figure 17. ROMS runs D1–D4: time series of (a) near surface temperature at 0.81 m depth and (b) mixed-layer depth, and the corresponding observations at mooring M1. The numbers on the abscissae indicate June dates. The instant of the last assimilation is marked by the black arrow in (a).
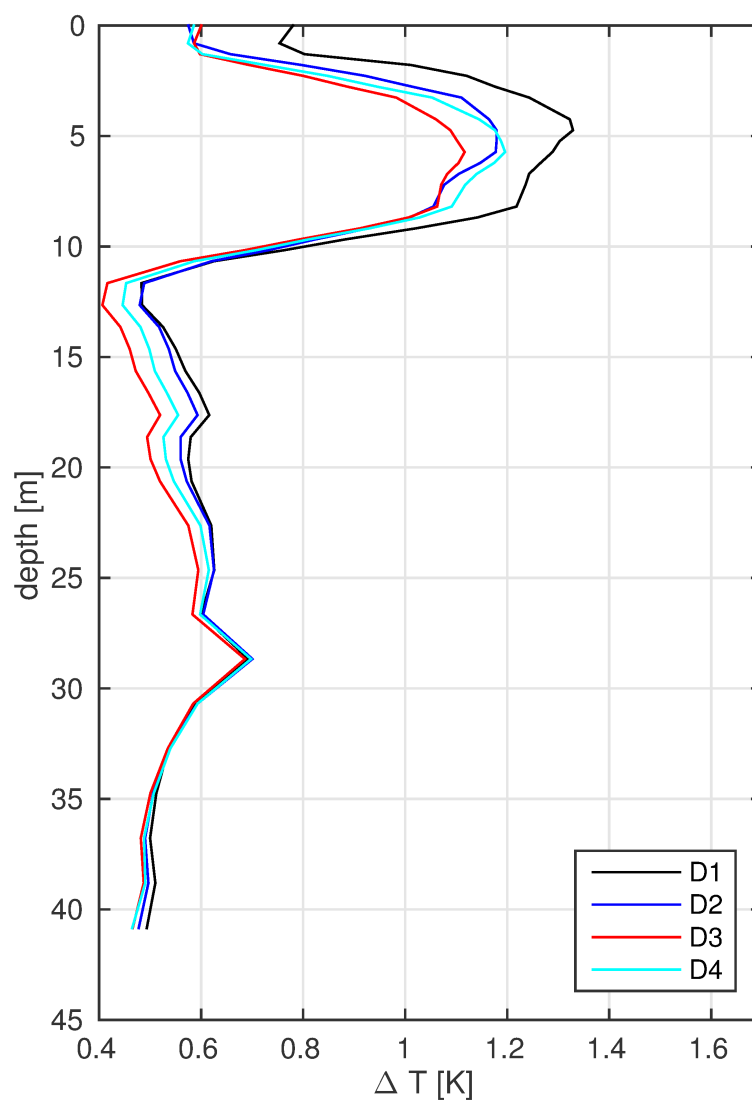
Figure 18. ROMS runs D1–D4: *rms* temperature differences ΔT [K] between the modelled temperature T_{ROMS} and the observed temperature T_{obs}, evaluated at the actual depths of the observations. ΔT was computed only for the period of time after 12 June 00:00h.
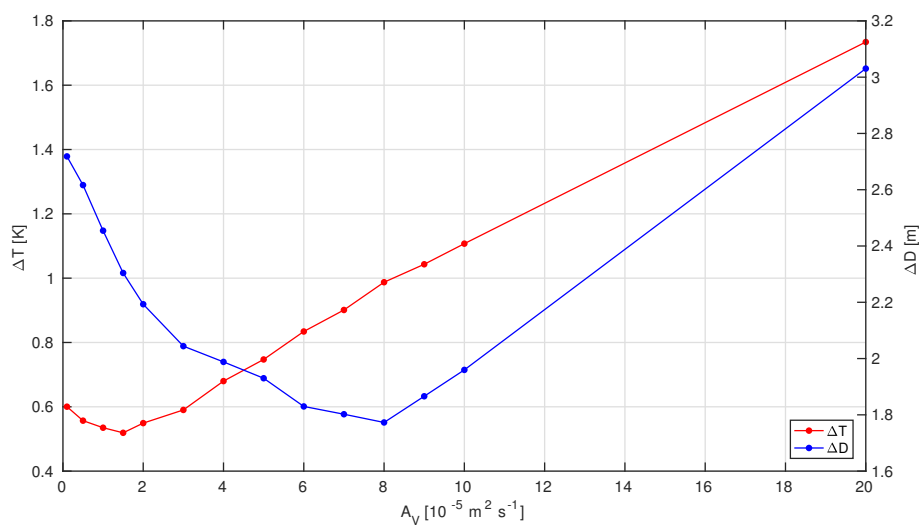
Figure 19. Series E: ΔT and ΔD for ROMS runs E1 – E14. Both quantities were computed only for the period of time after 12 June 00:00h.
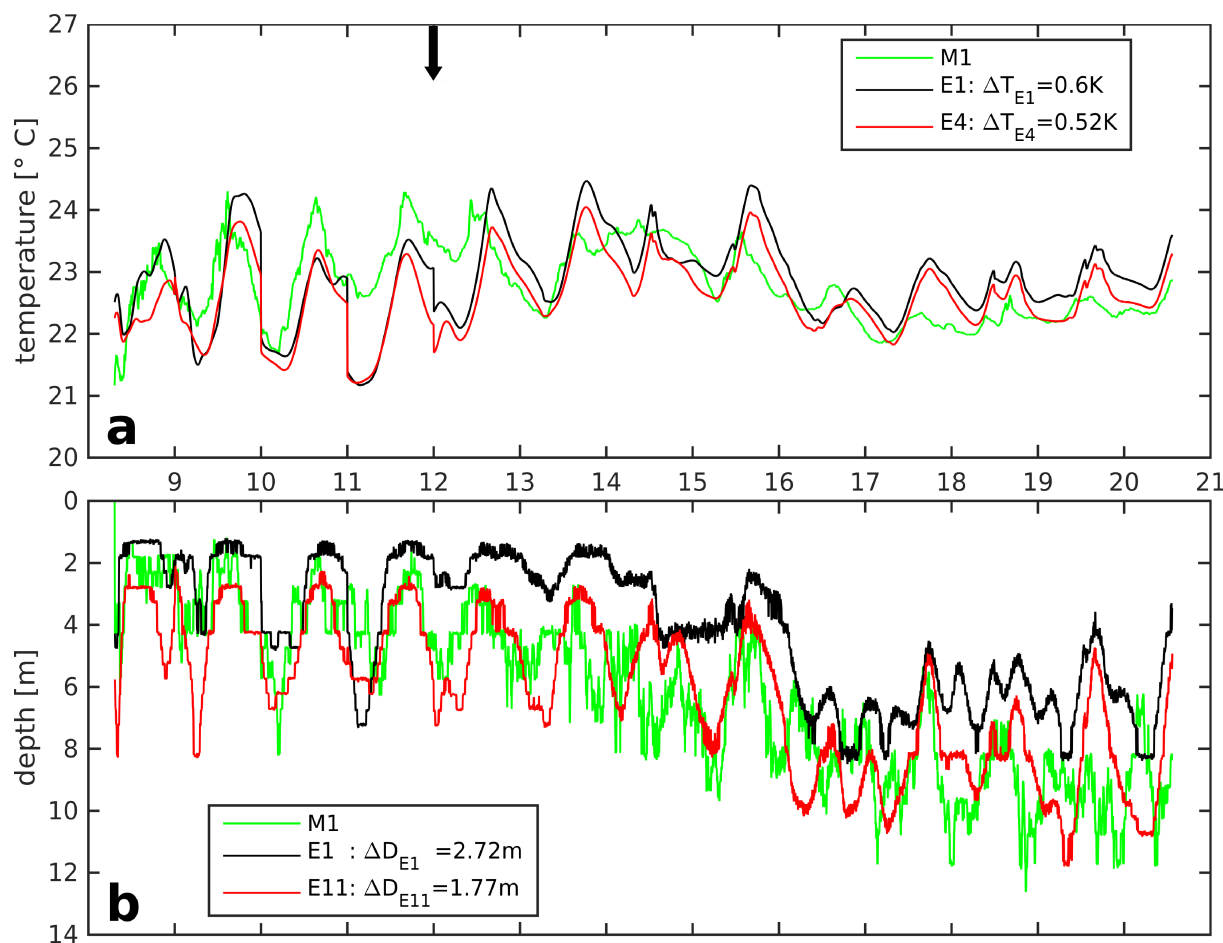
Figure 20. Time series of (a) near surface temperature at 0.81 m depth from E1, E4 and (b) mixed-layer depth from E1, E11, and the corresponding observations at mooring M1. The numbers on the abscissae indicate June dates. The instant of the last assimilation is marked by the black arrow in (a).
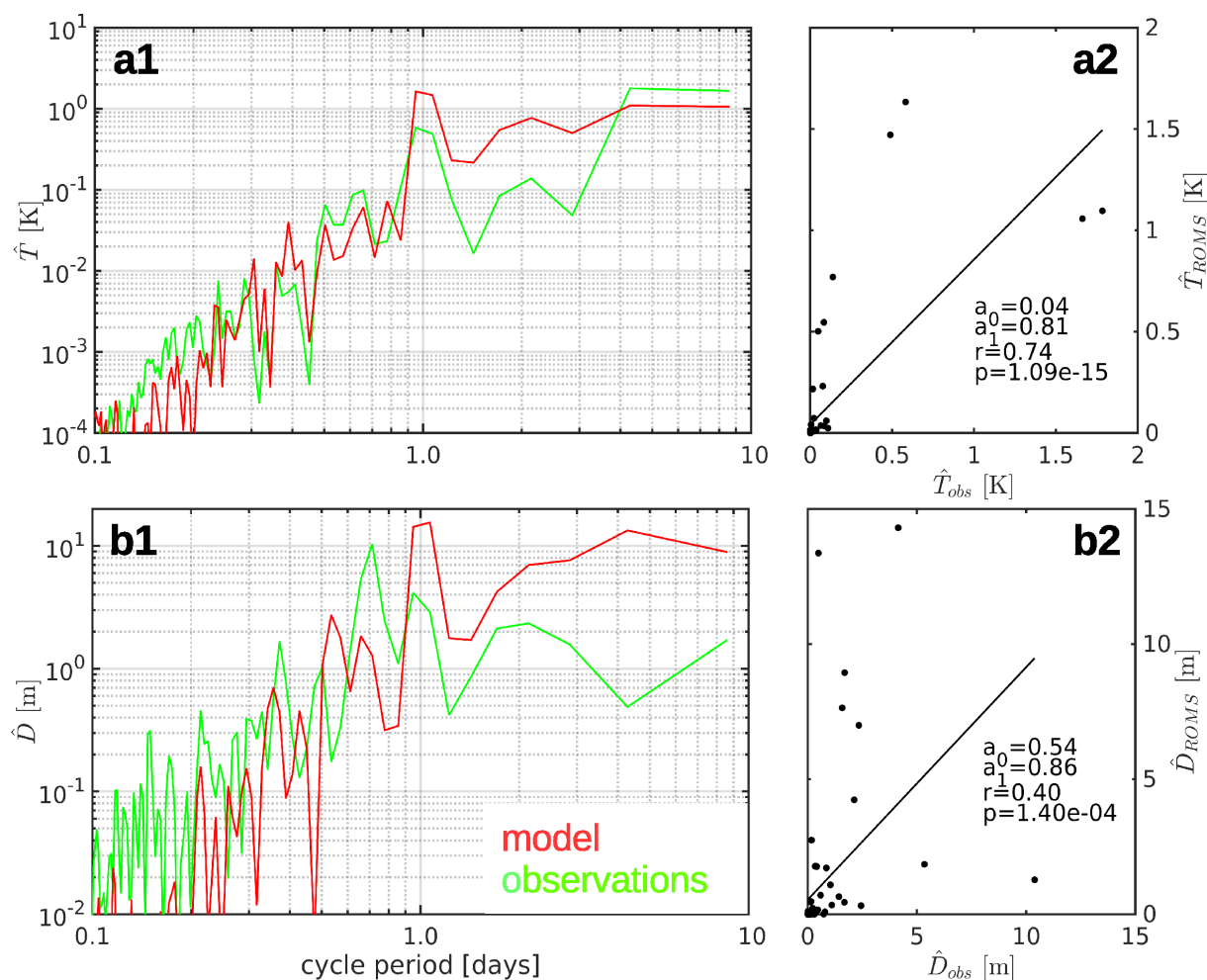
Figure 21. Spectra and correlation parameters of the modelled and observed amplitudes (a) $\hat{T}$ of the near-surface temperature at 0.81 m depth from run E4 and (b) $\hat{D}$ of the mixed-layer depth from run E11.
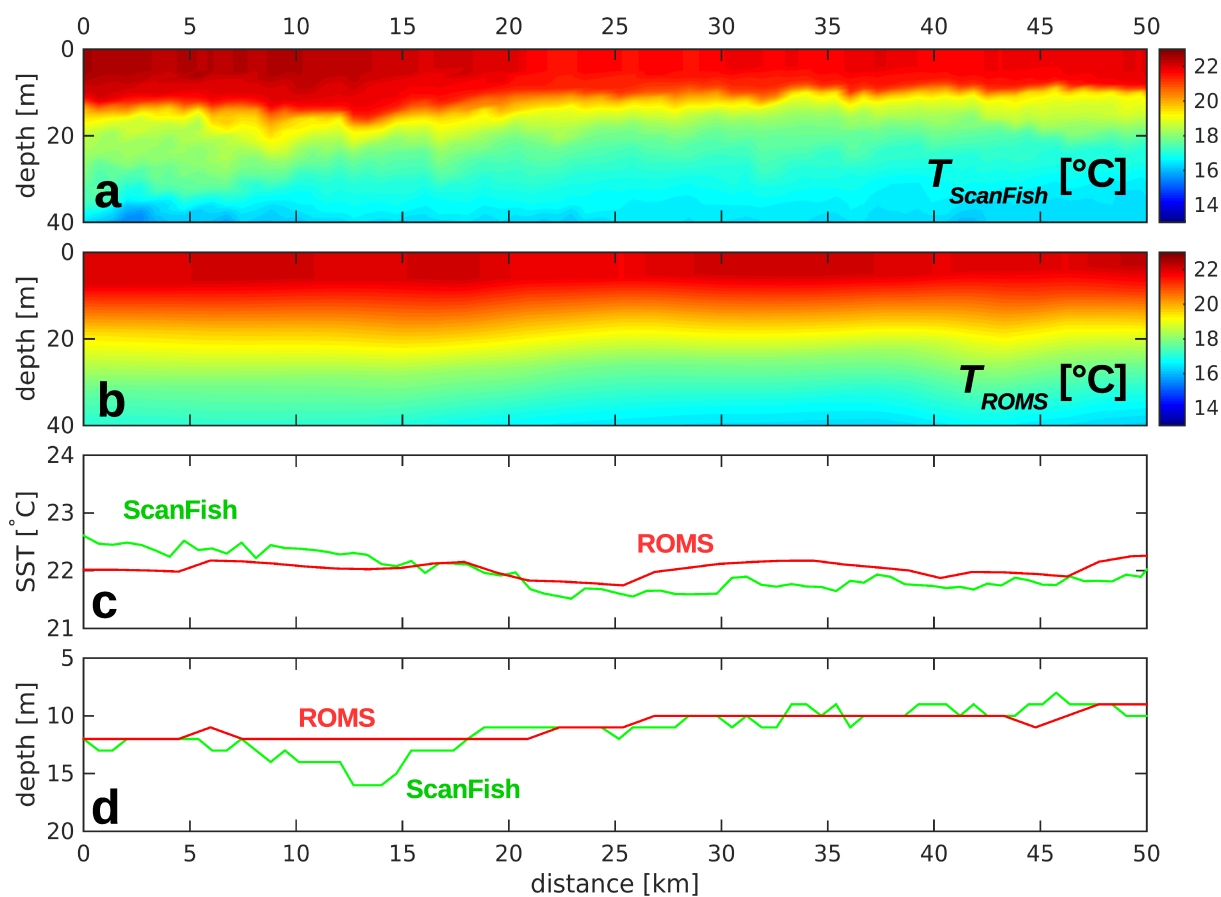
Figure 22. Sections along the A05 ScanFish track (cf. Fig. 4) at 40°48'N: (a) temperature recorded by the ScanFish, (b) temperature predicted by ROMS, (c) near-sea surface temperature SST, and (d) mixed-layer depth evaluated from ScanFish measurements and ROMS.